# 2

# Analysis of Observational $(T, S)$ Profiles

The P-vector method is to invert absolute velocity from hydrographic data and usually requires regularly distributed $(T, S)$. However, the $(T, S)$ fields are sampled irregularly in space and time. As a first step, the observational $(T, S)$ profiles should be analyzed. This chapter describes basic features of the observational $(T, S)$-profiles, two-type profile representations, thermal and haline parametric models, and decorrelation scales. There are many hydrographic data sets, however, only those data sets used in this book are described.

## 2.1 Historical $(T, S)$ Profiles

The MOODS is a compilation of ocean data observed worldwide consisting of (a) temperature-only profiles, (b) both temperature and salinity profiles, (c) sound-speed profiles, and (d) surface temperatures (drifting buoy). It contains the NODC temperature and salinity profiles. The measurements in the MOODS are, in general, irregular in time and space. Due to the shear size and constant influx of data to the Naval Oceanographic Office from various sources, quality control is very important. The primary editing procedure included removal of profiles with obviously erroneous location, profiles with large spikes (temperature higher than 35°C and lower than −2°C), and profiles displaying features that do not match the characteristics of surrounding profiles, such as profiles showing increase of temperature with depth. The MOODS contains more than six million profiles worldwide.

For example, after quality control the historical MOODS data contains 144,135 temperature and 13,768 salinity profiles for the South China Sea (5°S–25°N, 105°C–120°E) during 1930–1997 (Chu et al. 1997c). The main limitation of the MOODS data is its irregular distribution in time and space. Certain periods and areas are over sampled while others lack enough observations to gain any meaningful insights. Vertical resolution and data quality are also highly variable depending much on instrument type and sampling expertise. The monthly distributions of the total temperature (Fig. 2.1)

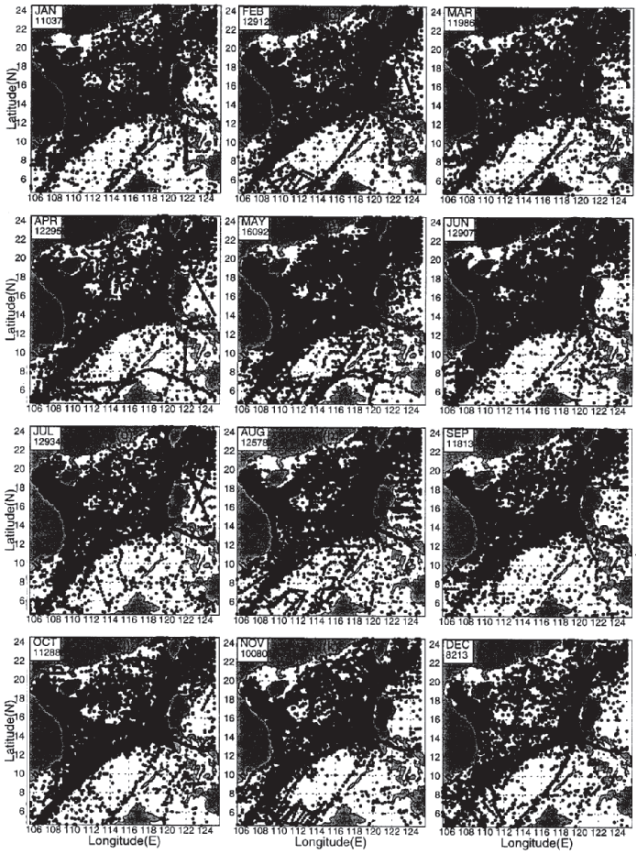


**Fig. 2.1.** Spatial distribution of the MOODS temperature stations during 1930–1997 (Chu and Li 2000, Journal of Physical Oceanography)

and salinity (Fig. 2.2) stations in the South China Sea show that the number of temperature stations is ten times more than the number of salinity stations.

Yearly temperature (Fig. 2.3a) and salinity (Fig. 2.3b) profile numbers show temporally uneven distribution with almost no observations in the whole South China Sea, in certain years (e.g., 1944 for temperature, and 1944–1946, 1952–1954, 1993–1995 for salinity) and many observations in other years (e.g., more than 12,000 temperature profiles in 1966 and 1968, and more than 1,100 salinity profiles in 1981). Spatial and temporal irregularities along with the lack of data in certain regions must be carefully weighted in order to avoid statistically induced variability.

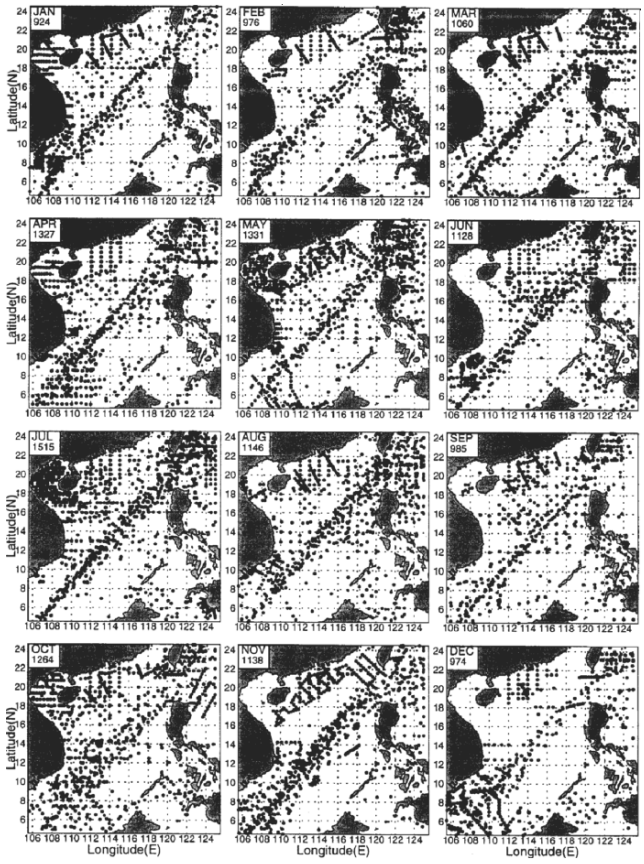


**Fig. 2.2.** Spatial distribution of MOODS salinity stations during 1930–1997 (Chu and Li 2000, Journal of Physical Oceanography)

## 2.2 Synoptic $(T, S)$ Profiles

Expendable bathythermograph (XBT) and conductivity-temperature-depth (CTD) are commonly used for hydrographic observations. Airborne XBT (AXBT) and CTD (AXCTD) surveys can cover greater geographic extents over shorter periods of time than ship surveys. The AXBT/AXCTD data sets, by virtue of their large spatial extents and the relatively short times required to complete them, essentially provide snapshots of thermal structure (AXBT) and thermohaline structure (AXCTD) over a large portion of water. The AXBT surveys are more frequent than the AXCTD survey.

For example, the Naval Oceanographic Office conducted an intensive AXBT survey between May 14 and May 25, 1995, over the majority of the South China Sea down to about 300 m depth. Figure 2.4 shows the daily AXBT deployment. This data set provides something close to a snapshot of the

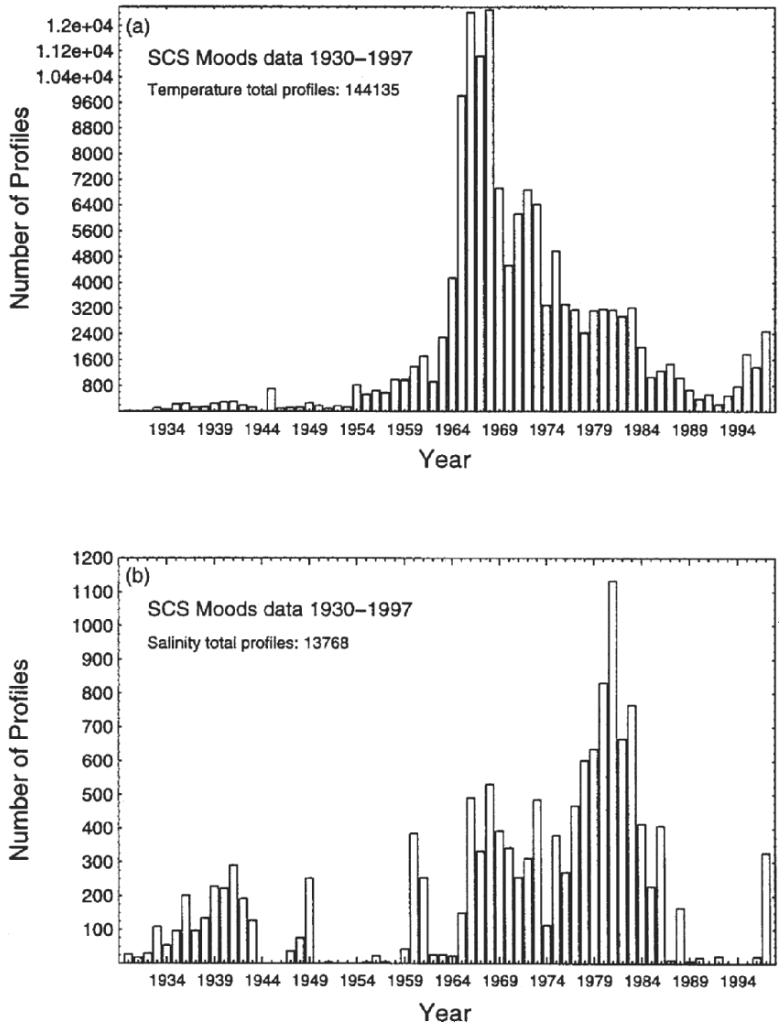


**Fig. 2.3.** Temporal distribution of the MOODS stations during 1930–1997: (**a**) temperature, and (**b**) salinity (Chu and Li 2000, Journal of Physical Oceanography)

temperature in the upper ocean in the South China Sea during the transition time before the onset of the monsoon. Most of the 376 AXBTs were deployed at six intervals over a 12-day period from May 14 to May 25, 1995. The majority of the AXBTs were nominally capable of reaching a depth of 360–400 m. The ensemble of temperature profiles (Fig. 2.5a) and the mean profile with an envelope of a standard deviation (Fig. 2.5b) show the existence of a mixed layer with depths ranging from 20 to 60 m and a thermocline with a vertical temperature gradient of 6°–7°C per 100 m below the mixed layer.

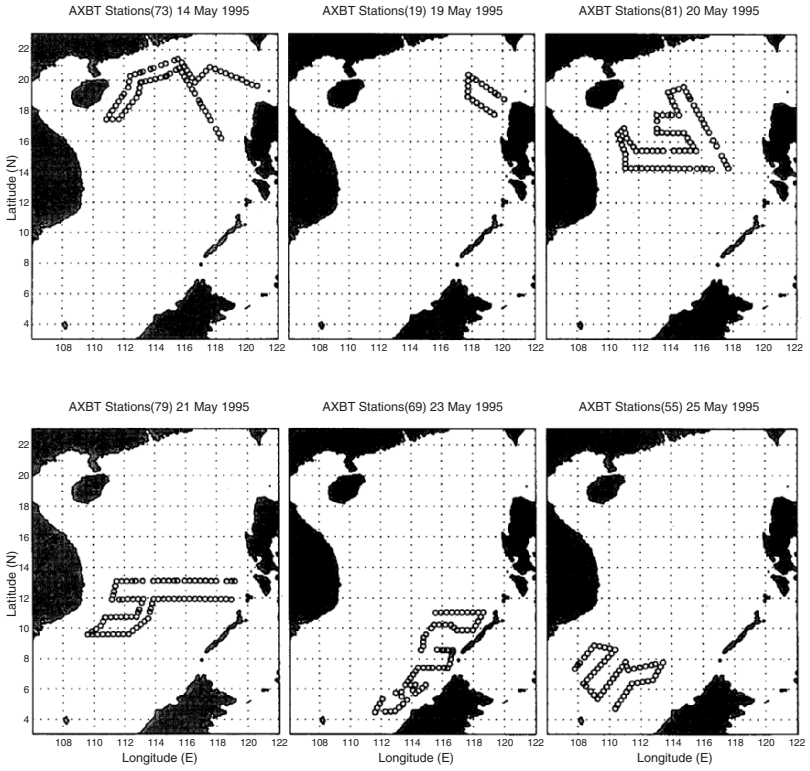


**Fig. 2.4.** Deployment of the AXBT survey in the South China Sea during 14–25 May 1995 (Chu et al. 1998d, Journal of Geophysical Research)

## 2.3 Representation of $(T, S)$ Profiles

Usually, the $(T, S)$ profiles for time $t$ are represented by

$$T_{\text{obs}} = T_k(z, t), S_{\text{obs}} = S_k(z, t), \tag{2.1}$$

where the subscript $k$ denotes the horizontal location. Two types are available in profile data analysis. First, the analysis is conducted at the same depth. This is the z-level analysis. Second, the profile data (2.1) can be represented by a set of parameters on the base of the physical characteristics (Chu et al. 1997a,b, 1999a). The analysis is conducted for each parameter. The parameter analysis is conducted as per the process given herewith.

The parameter analysis starts from analytical curve fitting of temperature and salinity profiles. Determination of thermohaline structure (mixed layer, entrainment zone, thermocline, and halocline) from observed temperature and salinity profiles is important for the world oceans for several reasons. First, the heat balance depends on the features of mixed layer, entrainment zone, and thermocline. Mixed layer deepens by entrainment of water from the ocean

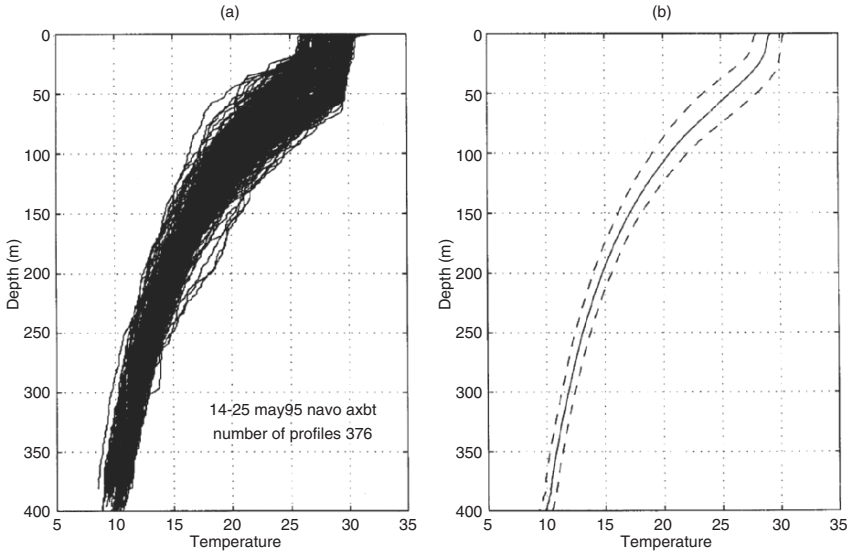


**Fig. 2.5.** Temperature profiles of the AXBT survey in the South China Sea during 14–25 May 1995 (after Chu et al. 1998d, Journal of Geophysical Research)

below (Chu 1988; Chu et al. 1990; Chu and Garwood 1990, 1991). The mass in the deep water is then transported to surface. Second, for polar oceans the mixed layer acts as a buffer by storing solar heat input during the summer and releasing it back to the ice throughout the fall and early winter (Maykut and McPhee 1995). Non-polar and polar parametric models are available for the analysis. For illustration, the Yellow Sea is taken as an example as the non-polar model, and the Beaufort/Chukchi Seas are taken as examples as the polar model.

## 2.4 Non-Polar Parametric Model

The Yellow Sea is a semi-enclosed basin covering roughly $295,000\,\mathrm{km}^2$ and is one of the most developed continental shelf areas in the world seas. While the Yellow Sea covers a relatively large area, it is quite shallow reaching a maximum depth of about 140 m (Fig. 2.6). The Yellow Sea temperature profiles are taken as an example as the single-structure pattern for illustration (Chu et al. 1997a,b, 2006c,e).

### 2.4.1 Seasonal Variability

The water depth over most of the area in the Yellow Sea is less than 50 m. The deepest water is confined to a north–south oriented trench which runs

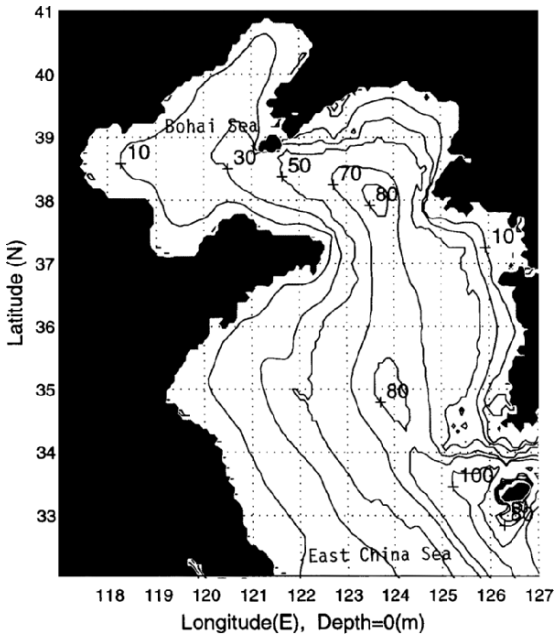


**Fig. 2.6.** Yellow Sea bathymetry (from Chu et al. 1997b, Journal of Geophysical Research)

from the northern boundary south to the 100 m isobaths, where it fans out onto the continental break. The gradients in slope across the bottom are very small. Such a broad and shallow continental shelf leads to the fact that the water is readily affected by seasonally varying atmospheric conditions such as heating, cooling, and wind stress. Therefore, the seasonal variation of the water masses is remarkably large (Chen et al. 1994). Another feature of the depth distribution is the east/west asymmetry. Extensive shoals (<20 m) are located in the western Yellow Sea along the Chinese coast and are not generally found in the South Korea coastal regions. Also, the 50 m isobaths is located more than 100 km from the Chinese coast, but only about 50 km from the South Korean coast. This asymmetry in bottom depth is important for the shoaling mixed layer depth. Furthermore, the hydrographic character of water masses in the Yellow Sea also depends on the degree of mixing of fresh water originating from the China Continent river run-off with the intrusion of East China Sea and Kuroshio waters (Park and Chu 2006b).

The Asian monsoon strongly affects the Yellow Sea thermal structure. During the winter monsoon season, a very cold northwest wind blows over the Yellow Sea as a result of the Siberian High Pressure System. The Jet Stream is positioned to the south of the Yellow Sea and the Polar Front to the north of Philippines. The mean surface wind speed over the Yellow Sea in January is nearly $6\,\mathrm{m\,s^{-1}}$. The sea surface temperature (SST) is 6°C at

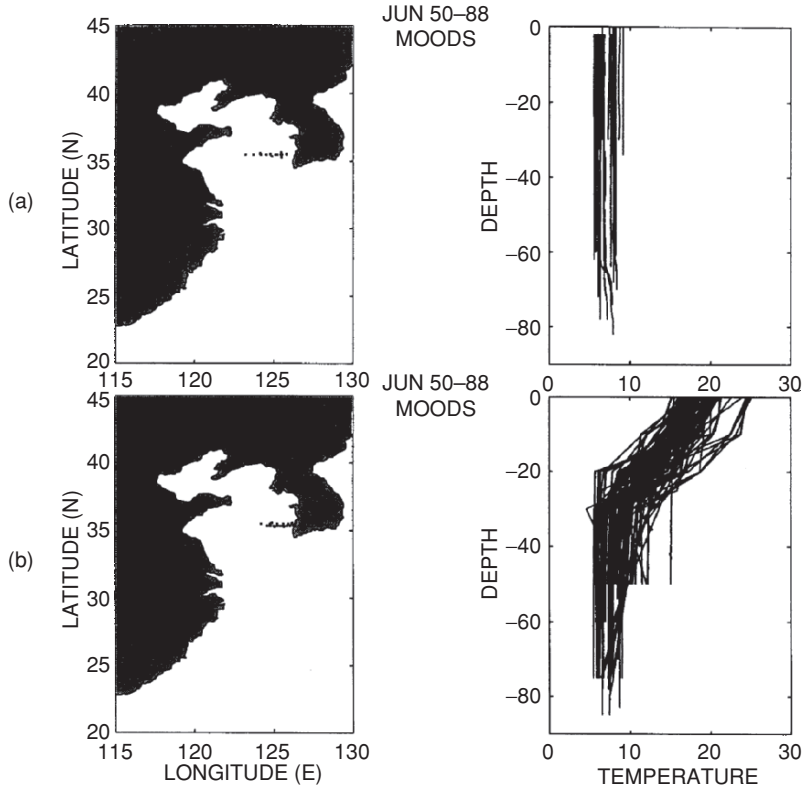


**Fig. 2.7.** Eastern Yellow Sea (around 36°N) temperature profiles during 1950–1988: (**a**) January and (**b**) June. *Solid dots* show the observational stations (from Chu et al. 1997b, Journal of Geophysical Research)

the northern extent and 10°C at the southeastern extent. The horizontal SST gradient largely impacts on the atmospheric circulation (Chu 1989).

January surface air temperature varies from 0 to 8°C in the Yellow Sea, roughly 2 to 6°C cooler than SST. The Yellow Sea surface loses heat to the atmosphere. The upward buoyancy flux at the air—ocean interface (thermal forcing), together with the strong wind stress (mechanical forcing), generates turbulence and mixes the surface water with the deeper water. Taking the eastern part of the Yellow Sea around 36°N as an example, the January historical (1950–1988) temperature profiles (Fig. 2.7a) show a single-layer structure (i.e., vertically uniform temperature from surface to the bottom). The different lengths of these profiles in the vertical temperatures are caused by the different water depths where the observations were taken (see Fig. 2.6). This single-layer structure means a very deep mixed-layer extending from the surface to the bottom.

In summer, the wind stress is much weaker than in winter. The monthly mean surface air temperature is quite uniform, around 24–26°C, and is usually 1.5–2°C warmer than the mean SST (Van Loon 1984). The warmer air causes a downward heat flux at the air–ocean interface. This heat flux along with the strong downward net radiation stabilizes the upper layer of the water and causes the surface mixed layer to shoal, creating a multi-layer structure (Fig. 2.7b). Below the thermocline, there is a cold water mass, commonly referred to as Yellow Sea Bottom Cold Water, that remains unchanged and nearly motionless throughout the summer (Li and Zeng 1992).

### 2.4.2 Model Description

During the summer monsoon season, most profiles in the Yellow Sea exhibit a mixed-layer (for temperature), a thermocline, and a deep layer (Fig. 2.7b), which can be outlined by a "typical" profile. To make the model more general, we assume two deep layers below the thermocline (Fig. 2.8). When the two deep layers have the same vertical gradients, they become one deep layer. If two transition layers are added, the entrainment zone between mixed layer and thermocline and the transition zone between the thermocline and the deep layer, the Yellow Sea thermal structure during summer can be well resolved. We use a parametric model with six layers (Chu 1995b; Chu et al. 1997b) to diagnose shallow-water multi-layer structure from observed Yellow Sea temperature profiles.

Each observed profile is modeled by a set of parameters, most of which have physical meaning, including SST, isothermal layer depth, depth of the base of the thermocline, gradient in the thermocline and deep layers, and additional parameters describing curvature between the mixed-layer and thermocline and curvature below the thermocline. Among them SST is taken as the observed values. The model parameters for each observed profile are computed in gradient space; more specifically, the depths and gradients of the modeled features are fit to the vertical gradient of the observed profile. The parametric model depicts the multi-layer structure. Determination of layer number is based on overall features of the profiles (Fig. 2.7b). The thermal parametric model consists of seven depths (i.e., six layers) and six gradients as shown in Fig. 2.8b. The first and the last depths are assumed to be at the surface and bottom, respectively, and the gradients within the isothermal layer and thermocline are constrained to be constant. The gradients for the four other layers are assumed to vary with depth linearly. The mean gradient is taken as the representative value for these layers. The model parameters are calculated in the gradient space, which will bring larger numerical errors due to the differentiation. We will use the optimization to filter out the noise.

If we consider profiles in the gradient space, i.e., $G_T = \partial T/\partial z$, each profile can be represented by the surface value (SST) along with the gradients,

$$[\mathrm{SST}, G_T(0, z_1), G_T(z_1, z_2), \ldots, G_T(z_{n-1}, z_n)] \,,$$

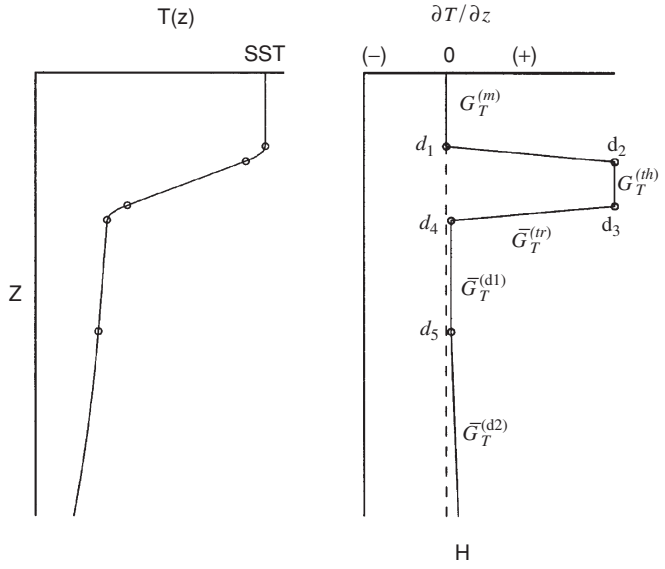


**Fig. 2.8.** Temperature and gradient space representations of the features or profile characteristics modeled by the parametric model (from Chu et al. 1997b, Journal of Geophysical Research)

for the temperature profiles. Here, $n+1$, is the number of data points, and $z_i\,(i = 1, 2, \ldots, n)$ are the depths of the sub-surface data points. For example, 100 temperature/depth points would produce 99 gradient values. If the surface value is included, we have the same amount of data in the gradient space as in the original data set.

On the basis of the continuity of $T$ and $\partial T/\partial z$ at interfaces of any two layers, a parametric model can be constructed as

$$\hat{T}^{(\mathrm{m})}(z) = G_T^{(\mathrm{m})} z + \mathrm{SST}, \quad z \in [-d_1, 0], \tag{2.2a}$$

$$\hat{T}^{(\mathrm{en})}(z) = \frac{(z+d_1)}{2(d_2-d_1)}\left[(G_T^{(\mathrm{th})} + G_T^{(\mathrm{m})})(d_2-d_1) - (G_T^{(\mathrm{th})} - G_T^{(\mathrm{m})})(z+d_2)\right]$$
$$+\hat{T}^{(\mathrm{m})}(-d_1), \quad z \in [-d_2, -d_1], \tag{2.2b}$$

$$\hat{T}^{(\mathrm{th})}(z) = G_T^{(\mathrm{th})}(z+d_2) + \hat{T}^{(\mathrm{en})}(-d_2), \quad z \in [-d_3, -d_2], \tag{2.2c}$$

$$\hat{T}^{(\mathrm{tr})}(z) = \frac{(z+d_3)}{(d_4-d_3)}\left[(G_T^{(\mathrm{th})} - \bar{G}_T^{(\mathrm{tr})})z + d_4 G_T^{(\mathrm{th})} - d_3 G_T^{(\mathrm{m})}\right]$$
$$+\hat{T}^{(\mathrm{th})}(-d_3), \quad z \in [-d_4, -d_3], \tag{2.2d}$$

$$\hat{T}^{(d1)}(z) = \hat{T}^{(\mathrm{tr})}(-d_4) + (z+d_4)\bar{G}_T^{(d1)} + \frac{(z+d_4)(z+d_5)}{(d_5-d_4)}[G_T^{(\mathrm{tr})}(-d_4) - \bar{G}_T^{(d1)}], \quad z \in [-d_5, -d_4], \tag{2.2e}$$

$$\hat{T}^{(d2)}(z) = \hat{T}^{(d1)}(-d_5) + (z+d_5)\bar{G}_T^{(d2)} + \frac{(z+d_5)(z+H)}{(H-d_5)}[G_T^{(d1)}(-d_5) - \bar{G}_T^{(d2)}], \quad z \in [-H, -d_5], \tag{2.2f}$$

where $\hat{T}^{(\mathrm{m})}, \hat{T}^{(\mathrm{en})}, \hat{T}^{(\mathrm{th})}, \hat{T}^{(\mathrm{tr})}, \hat{T}^{(d1)}$, and $\hat{T}^{(d2)}$ are modeled temperatures in the mixed-layer (or called isothermal layer), entrainment zone, thermocline, transition zone, and first and second deep layers. $H$ is the water depth, $d_1$ the mixed layer depth for temperature ($\mathrm{MLD}_T$), $d_2$ the depth of the top of thermocline, $d_3$ the depth of the bottom of thermocline, $d_4$ the depth of the top of the first deep layer, and $d_5$ the bottom of the first deep layer (Fig. 2.8). Here, we assume constant vertical temperature gradients in the ocean mixed-layer (very small, $G_T^{(\mathrm{m})} \simeq 0$) and in the thermocline (very large $G_T^{(\mathrm{th})}$), and linearly varying with $z$ in the entrainment zone, the transition zone, and the two deep layers with average values $\bar{G}_T^{(\mathrm{en})}, \bar{G}_T^{(\mathrm{tr})}, \bar{G}_T^{(d1)}$, and $\bar{G}_T^{(d2)}$. Here, the mean gradient in the entrainment zone is the average of the isothermal layer and thermocline gradients,

$$\bar{G}^{(\mathrm{en})} = \frac{1}{2}(G_T^{(\mathrm{m})} + G_T^{(\mathrm{th})}).$$

By forcing this parametric model (2.2) to each observed profile, we should have a first-guess of the five depths $(d_1, d_2, d_3, d_4, d_5)$ and a high resolution of temperature/depth points in the vertical gradient in order to obtain the five temperature gradients $(G_T^{(\mathrm{m})}, G_T^{(\mathrm{th})}, \bar{G}_T^{(\mathrm{tr})}, \bar{G}_T^{(d1)}, \bar{G}_T^{(d2)})$. Such a treatment provides the most important features from the observational data.

Each temperature profile is linearly interpolated to $\Delta z = 0.5\,\mathrm{m}, T_j = T(z_j)$, where $z_j = z_{j-1} - 0.5\,\mathrm{m}(z_0 = 0)$. If the five depths $(d_1, d_2, d_3, d_4, d_5)$ are known, the high resolution profile data set $(z_j, T_j)$ can be divided into six parts (isothermal layer, entrainment zone, thermocline, transition zone, first deep layer, and second deep layer). For each layer the data $(z_j, T_j)$ are fitted to the parametric model (2.2), and a set of temperature gradients $(G_T^{(\mathrm{m})}, G_T^{(\mathrm{th})}, \bar{G}_T^{(\mathrm{tr})}, \bar{G}_T^{(d1)}, \bar{G}_T^{(d2)})$ are obtained.

### 2.4.3 Iteration Method

A modeled profile with 0.5-m resolution can be established by using the parametric model (2.2) if the five depths $(d_1, d_2, d_3, d_4, d_5)$ are given. In reality, these depths are not known prior to processing the data and vary from one profile to the other. The iteration method is used to obtain the optimal modeled profile.

First, start with a set of first-guess values of the depths and the five gradients (two constants and three mean values),

$$D^{(0)} = [d_1^{(0)}, d_2^{(0)}, d_3^{(0)}, d_4^{(0)}, d_5^{(0)}],$$
$$G_T^{(0)} = [G_T^{(\mathrm{m0})}, G_T^{(\mathrm{th0})}, \bar{G}_T^{(\mathrm{tr0})}, \bar{G}_T^{(d10)}, \bar{G}_T^{(d20)}]. \tag{2.3}$$

For example, Chu et al. (1997b) chose,

$$D^{(0)} = [20\,\mathrm{m}, 24\,\mathrm{m}, 32\,\mathrm{m}, 38\,\mathrm{m}, H],$$
$$G_T^{(0)} = [0,\ 0.5^\circ\mathrm{C\ m^{-1}}, 0.05^\circ\mathrm{C\ m^{-1}}, 0, 0],$$

for the Yellow Sea thermal structure. Let $(z_j, \hat{T}_j^{(k)})$ be the $k$th iterated model profiles. For each high resolution profile, the 0th iterated model profile is easily obtained from the first guess depths and gradients (2.3). The root-mean-square error (rmse) for mismatch of $T_j$ and $\hat{T}_j^{(k)}$ is computed by

$$\mathrm{rmse}^{(k)} = \sqrt{\frac{1}{n}\sum_{j=1}^{n}(\hat{T}_j^{(k)} - T_j)^2}. \tag{2.4}$$

It is expected that $\mathrm{rmse}^{(0)}$ to be large.

Second, use the iteration method to obtain optimal modeled profile for each observed high resolution profile. Each depth can only be adjusted one vertical grid ($\Delta z$ or $-\Delta z$) for iteration. From the $k$th iteration ($k$ starting from 0, the first-guess) set of depths, $D^{(k)}$, we have 242 ($=3^5 - 1$) different combinations of the depth adjustment,

$$D_{\mathrm{m}}^{(k+1)} = D_{\mathrm{m}}^{(k)} + \delta D_{\mathrm{m}}^{(k)}, \tag{2.5}$$

where

$$\delta D_1^{(k)} = (\Delta z, 0, 0, 0, 0),$$
$$\delta D_2^{(k)} = (-\Delta z, 0, 0, 0, 0),$$
$$\cdots\cdots$$
$$\delta D_{242}^{(k)} = (0, 0, 0, 0, -\Delta z).$$

Equations (2.2a)–(2.2f) are used to obtain 242 modeled profiles, among which we pick a profile with minimum rmse as the $(k+1)$th iterated set of depths, $D^{(k+1)}$. This procedure is repeated until the minimum rmse is achieved. We have two check points to terminate the iteration: the maximum number of iterations $k_{\max}$, and the rms error criterion $R_{\mathrm{c}}$. At each iteration ($k < k_{\max}$), $\mathrm{rmse}^{(k)}$ is compared to a user specified criterion $R_{\mathrm{c}}$. If $\mathrm{rmse}^{(k)} < R_{\mathrm{c}}$, we terminate the iteration and obtain an optimal set of depths. If $\mathrm{rmse}^{(k)} > R_{\mathrm{c}}$, we continue the iteration until $k = k_{\max}$. If the rmse at the

$k_{max}$ iteration is still greater than $R_c$, we should reject the parametric model (2.2), i.e., the observed profile cannot be fitted by the parametric model. The rejected profiles are discarded.

Chu et al. (1997b) chose $k_{\max} = 400$, and $R_c = 0.4°C$. This rms criterion (0.4°C) was chosen due to the accuracy of the temperature/depth ($\pm 0.2°C, \pm 2\,m$) measured by the bathythermograph. This criterion can be greatly reduced if the data are obtained by more accurate instruments (e.g., thermometer). The six temperature gradients are updated each iteration. A set of their six optimal gradients is obtained when the rms error of the temperature profile is less than the criterion.

## 2.5 Polar Parametric Model

### 2.5.1 Seasonal Variability

The Chukchi Sea is a shallow sea with a mean depth of 40–50 m, having gentle knolls and several troughs which are shallow but with a relief which has a substantial fraction of the mean depth. The Beaufort Sea is a semi-enclosed basin with quite a narrow continental shelf (30–80 km) and a deep submarine canyon, the Mackenzie Canyon. The deepest water is confined to the bowl-shaped Mackenzie Canyon which is enclosed by the 3,000 m isobaths. The gradients in slope across the bottom are very large. The 150 m isobaths approximately characterizes the Beaufort Sea shelf break (Fig. 2.9). The shallow continental shelf waters are affected by seasonally varying atmospheric conditions such as heating, cooling, wind stress, and the formation and melting of ice. The seasonal variation of the water masses is remarkably large. Thus, we have two different types of profiles: (a) shelf profiles (water depth $\leq 150\,m$) and (b) deep water profiles (water depth $> 150\,m$).

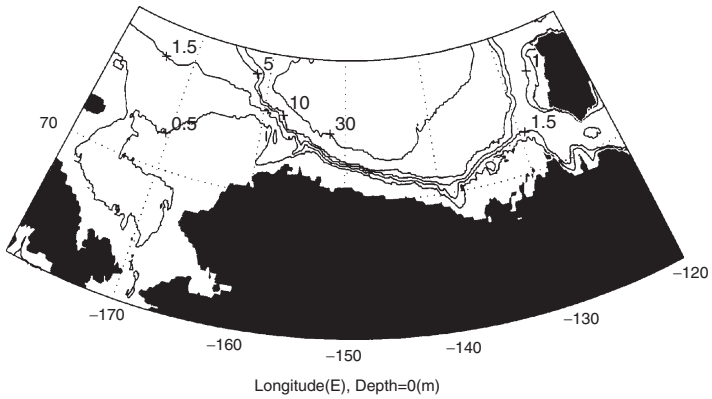


**Fig. 2.9.** The Beaufort/Chukchi Sea bathymetry. Numbers show the depth in 100 m (from Chu et al. 1999a, Journal of Atmospheric and Oceanic Technology)

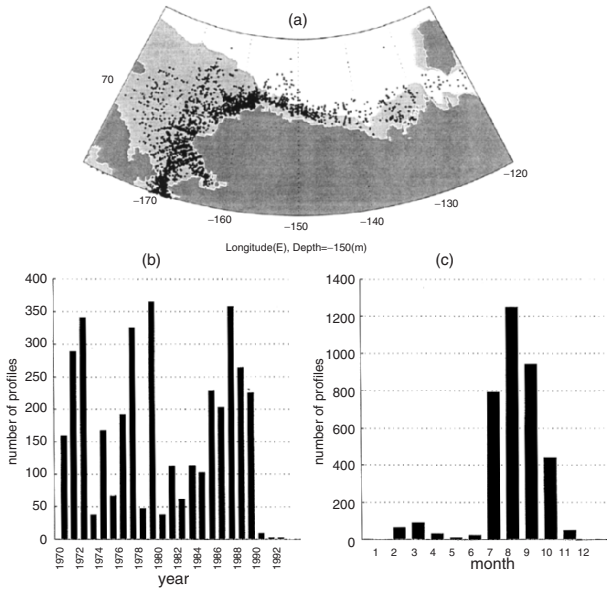


**Fig. 2.10.** The MOODS data for the Beaufort/Chukchi Sea: (**a**) station distribution, (**b**) interannual variation (1970–1993) of number of profiles, and (**c**) seasonal variation of number of profiles (from Chu et al. 1999a, Journal of Atmospheric and Oceanic Technology)

Among the historical (1970–1993) temperature and salinity profiles (3,562) obtained from the Naval Oceanographic Office, 3,384 profiles are shelf profiles, and 178 profiles are deep water profiles. For the area 120–180°W, 65–75°N, the MOODS (CTD and STD) has 3,562 $(T, S)$ profiles during 1970–1993 after rejecting certain data during quality control. These primary editing procedures included removal of profiles with obviously erroneous location, profiles with large spikes, poor vertical resolution, and profiles displaying features that do not match the characteristics of surrounding profiles.

There is a data sparse area north of 73°N (Fig. 2.10a). The periods of 1971–1972, 1977, 1979, and 1985–1989 are found to have a relatively large number profiles averaging around 200 profiles per year (Fig. 2.10b). Most profiles were observed during the summer season (Fig. 2.10c). August has the most observations (1,253) while no observations have been recorded in the data set in December and January.

The surface radiative flux strongly affects the Beaufort/Chukchi Sea shelf thermohaline structure. During the winter (November–April), long periods of darkness together with low solar elevation give rise to a prolonged period of radiative loss from the surface. The radiative cooling at the surface destabilizes the upper layer through strong upward heat flux and salt rejection by ice freezing, and causes the formation of deep mixed layer, which on the shallow

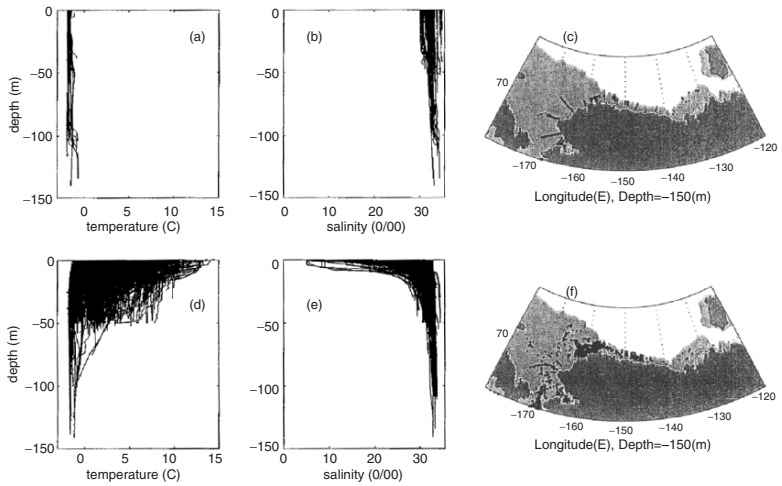


**Fig. 2.11.** Seasonal variation of $T, S$ profiles over the Beaufort/Chukchi Sea shelf water: (**a**) winter (November–April) $T$ profiles, (**b**) winter $S$ profiles, (**c**) distribution of winter stations, (**d**) summer (August) $T$ profiles, (**e**) summer $S$ profiles, and (**f**) distribution of summer stations. The shaded areas indicate shelf region (water depth $\leq 150$ m) (from Chu et al. 1999a, Journal of Atmospheric and Oceanic Technology)

shelves might reach the bottom resulting in an isothermal/isohaline structure (Figs. 2.11a,b).

Different lengths of these profiles in the vertical gradients are caused by the different water depths where the observations were taken (Fig. 2.9). During the summer (August), long daylight hours together with relatively high solar elevation give rise to a period of radiative deposition to the surface. The radiative warming at the surface stabilizes the upper layer through downward heat flux and fresh water influx by ice melting, causing the mixed layer to shoal and forming a multi-layered structure (i.e., a mixed-layer, upper and lower thermoclines and haloclines, and a deep layer), as shown in Figs. 2.11d,e. The number and spatial distribution of observations are much greater in summer than in winter (Figs. 2.11c,f).

In the deep water off the shelf the near surface waters of the Beaufort Sea also experience seasonal variations. During the winter (November– April), surface cooling causes the formation of a deep thermal mixed layer (Fig. 2.12a). However, the surface salt flux caused by local ice freezing generates a relatively shallow salinity mixed layer (Fig. 2.12b). Below both the thermal and salinity mixed layers there exists a lower thermocline and halocline, appearing at 160–300 m depth (Figs. 2.12a,b). During summer (August), surface warming and associated ice melting increase the SST (a maximum value near 8°C), decrease the sea surface salinity (a minimum value near 20 ppt), and cause both the thermal and salinity mixed layers to shoal (Figs. 2.12d,e). We also notice that both winter and summer stations (Fig. 2.12c,f) do not extend far from the

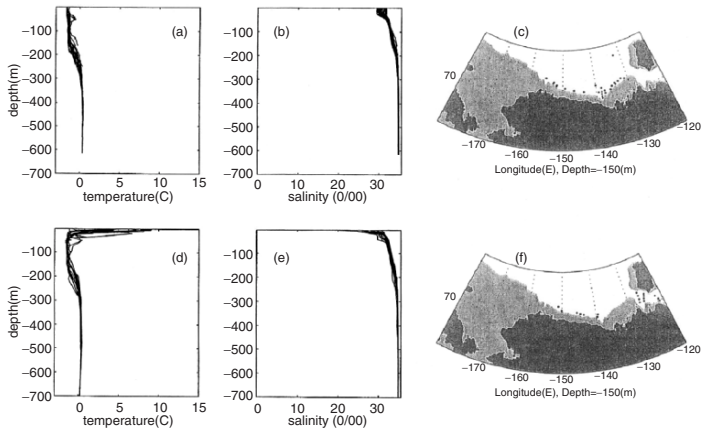


**Fig. 2.12.** Seasonal variation of $T, S$ profiles over the Beaufort/Chukchi Sea deep water: (**a**) winter (November–April) $T$ profiles, (**b**) winter $S$ profiles, (**c**) distribution of winter stations, (**d**) summer (August) $T$ profiles, (**e**) summer $S$ profiles, and (**f**) distribution of summer stations. The shaded areas indicate shelf region (water depth $\leq 150$ m) (from Chu et al. 1999a, Journal of Atmospheric and Oceanic Technology)

shelf break, and the intermediate waters (below 150 m depth) do not exhibit a seasonal variation.

### 2.5.2 Multiple Thermohaline Structures

The historical Beaufort/Chukchi Sea temperature and salinity profiles (Figs. 2.11 and 2.12) demonstrate the existence of several basic profile shapes which are deep mixing, shallow mixing, and advection.

(a) Deep mixing type (T, S) profiles. This type of T, S profiles is characterized by a single well-mixed layer in the shelf region (Fig. 2.13a) and a deep surface isothermal layer (Fig. 2.14a) and a thermocline in the deep water region. This type of T, S profiles are caused by surface destabilization, such as strong wind forcing, surface cooling, and brine rejection due to ice freezing. They are most prevalent during winter.

(b) Shallow mixing type (T, S) profiles. This type of T, S profiles is characterized by a multi-layered structure: shallow isothermal layer, isohaline layer (or called mixed layer for salinity), entrainment zone, thermoclines and haloclines, and a sub-layer in both the shelf region (Figs. 2.13b,d) and the deep water region (Figs. 2.14b,d). This profile type is generally present during the summer and is caused by surface stabilization, such as weak wind forcing, surface warming, and fresh water influx due to ice melting and river run-off, and therefore usually has a warm SST and a low sea surface salinity.

Beneath the mixed layer the thermocline/halocline profile is complex reflecting the seasonal adjustment. Thus, shallow mixing profiles feature a monotonic decrease of temperature with depth in the upper thermocline and a

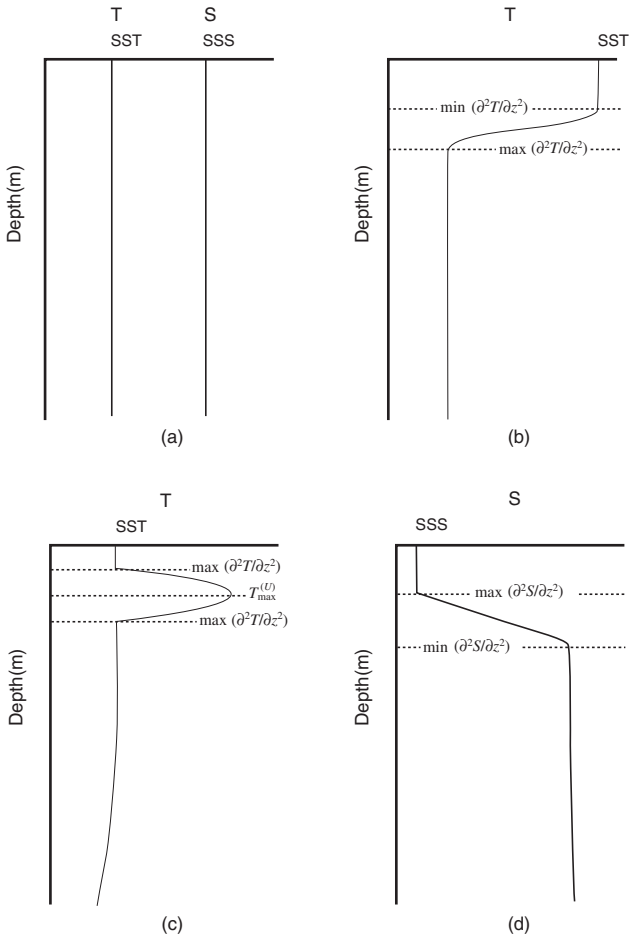


**Fig. 2.13.** Typical $T, S$ profiles for the shelf water: (**a**) deep-mixing type, (**b**) shallow-mixing type $T$, (**c**) advection type $T$, and (**d**) shallow-mixing type $S$ (from Chu et al. 1999a, Journal of Atmospheric and Oceanic Technology)

monotonic increase of salinity with depth in the upper halocline (Figs. 2.13b,d and 2.14b,d).

(c) Advection type T-profiles. Advection type $T$ profiles also have a multi-layer structure (shallow isothermal and isohaline layers, entrainment zone, upper and lower thermoclines, and a sub-layer) in both the shelf region (Fig. 2.13c) and the deep water region (Fig. 2.14c).

This type of profiles, identified by a nose-shape curve in the upper thermocline (monotonic increasing $T$ with depth to a maximum value $T_{\max}$ and then monotonic decreasing with depth), is generated by a prominent hydrographic feature on the Beaufort Sea shelf: a sub-surface temperature maximum,

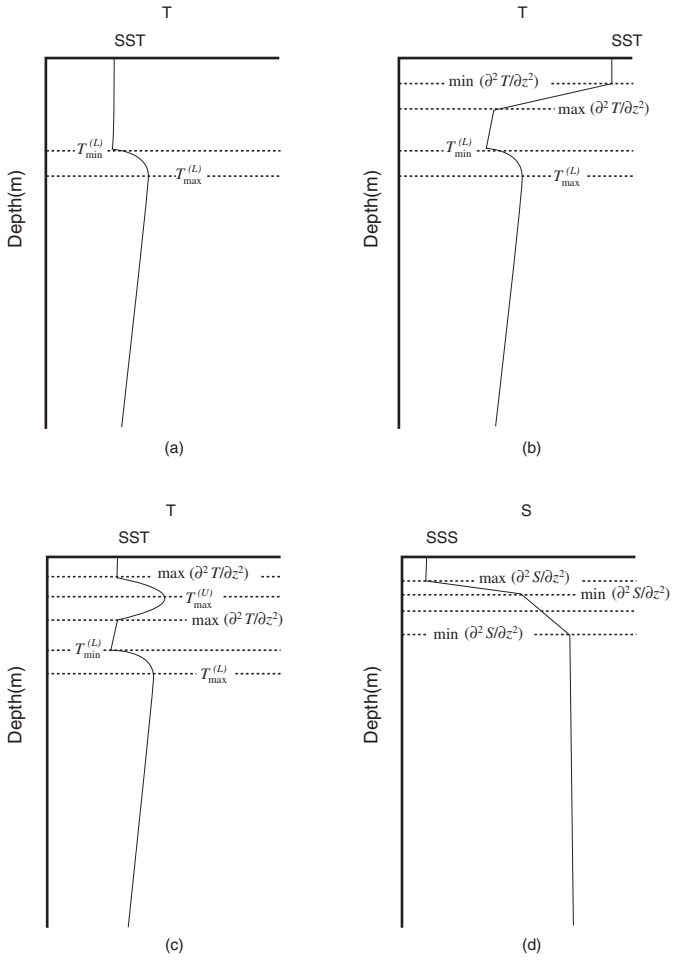


**Fig. 2.14.** Typical $T, S$ profiles for the deep water: (**a**) deep-mixing type $T, S$, (**b**) shallow-mixing type $T$, (**c**) advection-type $T$, and (**d**) shallow-mixing type $S$ (from Chu et al. 1999a, Journal of Atmospheric and Oceanic Technology)

generally found at about 20–30 m depth in the deep water and at about 10 m depth in the shelf water. This temperature maximum is associated with the eastward flowing Bering Sea water (Coachman and Barnes 1961; Aagaard 1989). The warm water that enters the Beaufort Sea comes through the eastern Bering Strait and follows the Alaskan coast around Point Barrow. Mountain et al. (1976) identified this warm intrusion as the combination of the two water masses: warm (5–10°C) and fresh (salinity below 31.5 ppt) Alaskan Coastal Water, and more saline Bering Sea Water. The two water masses mix rapidly with the ambient surface water as they move eastward. Aagaard (1989) estimated that the Alaskan Coastal Water is not clearly identifiable east of

147–148°W, and the Bering Sea Water east of 143°W. Thus, the longitude of 141°W is chosen as the separation for the western and eastern parts of the Beaufort Sea Shelf Water.

### 2.5.3 Characteristics from Profiles

(a) Heterogeneous mesh difference scheme. Second derivatives $\partial^2 F(z_j)/\partial z^2$ ($F$ is $T$ or $S$) are used to describe the features of profiles and to identify various types of $T$, $S$ profiles in the polar region. For each profile (temperature or salinity), $F(z_j), j = 1, 2, \ldots, N$, the following heterogeneous mesh difference scheme is used for the second-order derivatives,

$$\frac{\partial^2 F}{\partial z^2}|_{z_j} \simeq \frac{1}{z_{j+1} - z_{j-1}}\left(\frac{F_{j+1} - F_j}{z_{j+1} - z_j} - \frac{F_j - F_{j-1}}{z_j - z_{j-1}}\right), \tag{2.6}$$

where $j = 1$ refers to the surface, with increasing values indicating downward extension of the measurement. Equation (2.6) shows that two neighboring values, $F_{j-1}$ and $F_{j+1}$, are needed to compute the second-order derivative at $z_j$. For $j = 1, N$, the next point value is used, i.e.,

$$\frac{\partial^2 F}{\partial z^2}|_{z_1} = \frac{\partial^2 F}{\partial z^2}|_{z_2}, \quad \frac{\partial^2 F}{\partial z^2}|_{z_N} = \frac{\partial^2 F}{\partial z^2}|_{z_{N-1}}. \tag{2.7}$$

After the second-order difference is computed, we can use the following model to determine the top and bottom of the upper thermocline and halocline.

(b) Features of the shelf water profiles. Three types of profiles (deep-mixing, shallow-mixing, and advection) are found in the shelf water. The deep-mixing $T$, $S$ profiles reveal a single layer structure (Fig. 2.13a), i.e., the surface mixed layer extends to the bottom of the shelf (vertically uniform). The shallow-mixing $T$-profiles are characterized by a minimum/maximum of $\partial^2 T/\partial z^2$ at the top/bottom of the thermocline. Thus, the depths of the first minimum and the first maximum of $\partial^2 T/\partial z^2$ are taken as the top, $d_1^{(\mathrm{T})}$, and the bottom, $d_2^{(\mathrm{T})}$, of the thermocline (Fig. 2.13b).

The advection-type $T$-profiles are depicted by maxima of $\partial^2 T/\partial z^2$ at both top of the upper thermocline and bottom of the lower thermocline and a depth, $d_{\max}^T$, with the maximum temperature $T_{\max}^U$. The depths of the first and second maxima of $\partial^2 T/\partial z^2$ are taken as top,$d_1^T$, and bottom, $d_2^T$, of the upper/lower thermoclines (Fig. 2.13c).

The shallow-mixing type $S$-profiles are featured by a maximum/minimum of $\partial^2 S/\partial z^2$ at top/bottom of the halocline. From the ocean surface downward, the depths of the first maximum and the first minimum of $\partial^2 S/\partial z^2$ are taken as top,$d_1^T$, and bottom, $d_2^T$, of the halocline (Fig. 2.13d).

(c) Features of the deep water profiles. The deep-mixing type $T$-profiles reveal a thick surface mixed layer (Fig. 2.14a) above a positive gradient thermocline. The shallow-mixing type $T$-profiles are characterized by a minimum/maximum of $\partial^2 T/\partial z^2$ at top/bottom of the upper thermocline. Thus,

the depths of the first minimum and the first maximum of $\partial^2 T/\partial z^2$ are taken as top, $d_1^T$, and bottom, $d_2^T$, of the upper thermocline (Fig. 2.14b). Below the upper thermocline, a region of cold, nearly isothermal water exists which is a remnant of the previously cooling and convective mixing of water. Beneath this isothermal layer, there is a positive gradient lower thermocline similar to that described by the deep-mixing profiles.

The advection type $T$-profiles are depicted by maxima of $\partial^2 T/\partial z^2$ at both top and bottom of the upper and lower thermoclines and at a depth,$d_{\max}^T$, with a maximum temperature $T_{\max}^U$. The depths of the first and second maxima of $\partial^2 T/\partial z^2$ are taken as top, $d_1^T$, and bottom, $d_2^T$, of the upper thermocline (Fig. 2.14c). Below the depth of intrusion of warm Bering Sea water, the temperature profile is similar to that described by the deep-mixing profiles.

The shallow-mixing type $S$-profiles are characterized by a maximum/minimum of $\partial^2 S/\partial z^2$ at top/bottom of the upper halocline. From the ocean surface downward, the depths of the first maximum and the first minimum of $\partial^2 S/\partial z^2$ are taken as the top, $d_1^S$, and bottom, $d_2^S$, of the upper halocline (Fig. 2.14d). A lower halocline, when present, is often concurrent with the positive thermocline of the shallow-mixing type $T$-profile and is characterized by a minimum of $\partial^2 S/\partial z^2$ at the lower halocline.

(d) Mixed layer depth. MLD for temperature and salinity is usually estimated by $d_1^F$,

$$\mathrm{MLD}_F = d_1^F. \tag{2.8}$$

When $d_1^F$ tends to an infinitesimally small depth ($d_1^F \simeq 0$), the upper thermocline (halocline) reaches the surface and the surface mixed layer disappears. Such profiles may be called stratified layers and treated as special case of the ordinary shallow-mixing or advection type profiles.

(e) Lower thermocline. The lower thermocline appears in the Beaufort Sea Deep Water. The major feature of $T$-profiles is the existence of minimum and maximum temperatures below the upper thermocline for the shallow-mixing and advection type profiles (Figs. 2.14b,c),

$$T_{\min} = \min_{z<-d_2^T} T(z), \quad T_{\max} = \max_{z<-d_2^T} T(z), \tag{2.9}$$

$$d_3^T = -\{z|T(z) = T_{\min}\}, \tag{2.10}$$

$$d_4^T = -\{z|T(z) = T_{\max}\}, \tag{2.11}$$

where $d_3^T$ and $d_4^T$ are the depths of the minimum and maximum temperatures below the upper thermocline, the corresponding data are $T(-d_3^T)$ and $T(-d_4^T)$. The layer between $d_3^T$ and $d_4^T$ may be identified as the lower thermocline. Usually, between the upper and lower thermoclines there exists a transition zone with a very weak vertical gradient.

### 2.5.4 Vertical Gradients

After the four depths,$d_1^F$, $d_2^F$, $d_3^F$, and $d_4^F$, are determined ($F$ is $T$ or $S$), some important physical parameters can be obtained from each $T$, $S$ profile.

(a) Isothermal and isohaline layers. The water above the depth of $d_1^F$ is taken as the mixed layer. Within the isothermal (isohaline) layer, the temperature (salinity) is assumed to be uniform with depth, i.e., the mixed layer temperature is the same as theSST,

$$\hat{F}(z) = F(0), \quad -d_1^F < z \leq 0. \tag{2.12}$$

(b) Entrainment zone. The entrainment zone below the mixed layer is assumed to be infinitesimally thin near the depth of $d_1^F$. The temperature (salinity) at the top of the entrainment zone is the same as the mixed layer temperature, and the temperature (salinity) at the bottom of the entrainment zone equals the temperature (salinity) at the top of the thermocline. Therefore, the temperature and salinity jump across the entrainment zone is represented as

$$\Delta F = F(0) - F(-d_1^F). \tag{2.13}$$

(c) Upper thermocline and halocline. The upper thermocline and halocline are located between $z = -d_1^F$ and $z = -d_2^F$. Vertical gradients of the upper thermocline ($G_{\text{th}}^U$) and halocline ($G_{\text{ha}}^U$) for the shallow mixing type $T$, $S$ profiles are,

$$G_{\text{th}}^U = \frac{T(-d_1^T) - T(-d_2^T)}{d_2^T - d_1^T}, \quad G_{\text{ha}}^U = \frac{S(-d_1^S) - S(-d_2^S)}{d_2^S - d_1^S}. \tag{2.14}$$

The vertical gradient of the upper thermocline ($G_{\text{th}}^U$) for the advection type $T$-profiles is estimated by

$$G_{\text{th}}^U = \frac{1}{2}\left[\frac{\left|T(-d_1^T) - T(-d_{\max}^T)\right|}{d_{\max}^T - d_1^T} + \frac{\left|T(-d_{\max}^T) - T(-d_2^T)\right|}{d_2^T - d_{\max}^T}\right]. \tag{2.15}$$

(d) Lower thermocline and halocline. The lower thermocline and halocline are located between $z = -d_3^F$ and $z = -d_4^F$. Vertical gradients of the lower thermocline ($G_{\text{th}}^L$) and halocline ($G_{\text{ha}}^L$) are estimated by

$$G_{\text{th}}^L = \frac{T(-d_3^T) - T(-d_4^T)}{d_4^T - d_3^T}, \quad G_{\text{ha}}^L = \frac{S(-d_3^S) - S(-d_4^S)}{d_4^S - d_3^S}. \tag{2.16}$$

### 2.5.5 Thermohaline Parametric Description

The thermohaline parametric model turns any profile into physical parameters: four depths $(d_1^F, d_2^F, d_3^F, d_4^F)$, temperature or salinity jump $\Delta F$, upper and lower thermocline (halocline) strength. Taking shallow-mixing type $(T, S)$ profiles as an example (remember that the deep-mixing type is a special case of the shallow-mixing type), the thermohaline parametric model is represented by

$$\begin{aligned}
\hat{F}(z) &= F(0), && -d_1^F < z \le 0, \\
\hat{F}(z) &= F(-d_1^F) - \tfrac{z+d_1^F}{d_2^F - d_1^F}[F(-d_2^F) - F(-d_1^F)], && d_2^F \le z \le -d_1^F, \\
\hat{F}(z) &= F(-d_2^F) - \tfrac{z+d_2^F}{d_3^F - d_2^F}[F(-d_3^F) - F(-d_2^F)], && -d_3^F \le z \le -d_2^F, \\
\hat{F}(z) &= F(-d_3^F) - \tfrac{z+d_3^F}{d_4^F - d_3^F}[F(-d_4^F) - F(-d_3^F)], && -d_4^F \le z \le -d_3^F, \\
\underline{c}\,\hat{F}(z) &= F(-d_4^F) - \tfrac{z+d_4^F}{d_N^F - d_4^F}[F(-d_N^F) - F(-d_4^F)], && -d_N^F \le z \le -d_4^F,
\end{aligned} \tag{2.17}$$

which is vertically uniform in the mixed layer and piecewise linear with depth below the mixed layer to the deepest depth of the observational point, $z = -d_N^F$. Note that the "model profile" takes the value of $F(-d_1^F)$ at the mixed layer base $z = -d_1^F$.

The advection type profiles can also be represented by (2.17) except for the upper thermocline $(-d_2^T \le z \le -d_1^T)$ which should be parameterized by

$$\hat{T}(z) = T(-d_1^F) - \frac{z + d_1^T}{d_{\max}^T - d_1^T}[T(-d_{\max}^T) - T(-d_1^T)], \quad -d_{\max}^T \le z \le -d_1^T,$$

$$\hat{T}(z) = T(-d_{\max}^F) - \frac{z + d_{\max}^T}{d_2^T - d_{\max}^T}[T(-d_2^T) - T(-d_{\max}^T)], \quad -d_2^T \le z \le -d_{\max}^T, \tag{2.18}$$

where

$$T(-d_{\max}^T) = T_{\max}^U.$$

### 2.5.6 Statistical Tests

For any profile, $F(z_j)$, $j = 1, 2, \ldots, N$, using (2.17) or (2.17) and (2.18), we obtain a corresponding model profile, $\hat{F}(z_j)$. Both $F(z_j)$ and $\hat{F}(z_j)$ have the same values at the depths 0, depths $-d_1^F, -d_2^F, -d_3^F, -d_4^F$, and $-d_N^F$, but do not necessarily have the same values at the other observational depths. If $\hat{F}(z_j)$ fits $F(z_j)$ well, the difference $\delta F(z_j) = F(z_j) - \hat{F}(z_j)$ should be very small at all observational points. We need to test if the difference is small enough to be neglected. The first test ($t$-test) is used to justify whether the mean value of $\delta F(z_j)$ is taken as zero. The second test (correlation test) is utilized to see if $\hat{F}(z_j)$ correlates well with $F(z_j)$.

After calculating the mean and standard deviation of $\delta F(z_j)$,

$$\overline{\delta F} = \frac{1}{N}\sum_{j=1}^{N}\delta F(z_j), s^2_{\delta F} = \frac{1}{(N-1)}\sum_{j=1}^{N}[\delta F(z_j) - \overline{\delta F}]^2, \tag{2.19}$$

we begin with the null hypothesis that $\overline{\delta F}$ is zero. The significance level ($\alpha$) is the probability that the given value of

$$t = \frac{\overline{\delta F}}{s_{\delta F}/\sqrt{N}} \tag{2.20}$$

is exceeded purely by chance. This value satisfies the $t$-distribution with $(N-1)$ degrees of freedom. If $|t| > t_{\alpha,N-1}$, we reject the null hypothesis, the modeled profile $\hat{F}(z_j)$ does not fit the observed profile $F(z_j)$ and should be rejected.

After a modeled profile $\hat{F}(z_j)$ passes the $t$-test, we start with the null hypothesis that $\hat{F}(z_j)$ does not correlate with the observation $F(z_j)$. The significance level ($\alpha$) is the probability that the given value of

$$\mu = \frac{\sum_{j=1}^{N}\left|\hat{F}(z_j) - \bar{\hat{F}}\right|^2}{\sum_{j=1}^{N}\left|\hat{F}(z_j) - F(z_j)\right|^2/(N-2)} \tag{2.21}$$

is not exceeded purely by chance. This value satisfies the $F$-distribution with $(1, N-2)$ degrees of freedom. If $\mu > F_\alpha(1, N-2)$, we reject the null hypothesis and conclude that the modeled profile $\hat{F}(z_j)$ does correlate with the observation $F(z_j)$.

## 2.6 Curve-Fitting Model

In the thermohaline parametric models described in Sects. 2.3 and 2.4, temperature and salinity are vertically continuous, but their gradients are discontinuous at the layer transition. If the vertical gradients are required continuous, we need to use a curve-fitting model. The basic concept of this model is to determine a set of analytical curves (mathematical expressions with parameters) that represent the vertical distribution of $T, S$ profiles. Different families of representative curves have been chosen for three sub-models, shallow top, mid-depth, and deep ranges, with each chosen such that the number of parameters required would yield a smooth profile. The matching conditions through the depth range transitions are chosen so that no discontinuities in vertical gradients occur. This requires overlapping of the two connected layers. For example, in constructing the US Navy's Generalized Digital Environmental Model (GDEM), Teague et al. (1990) suggested division of three sub-models as follows: shallow top sub-model (0–400 m), mid-depth sub-model (200–2,450 m), and deep sub-model (2,000 m to bottom).

### 2.6.1 Top Shallow Sub-Model (0–400 m)

The basic functional form used in GDEM to fit the top 400 m of temperature (top most temperature profile) is the squared amplitude response of the Butterworth filter (Oppenheim and Schafer 1975). This expression describes the vertical profile from the surface ($z = 0$) to the base of the seasonal thermocline (i.e., $z = -d$). It is then merged with an exponential tail which extends the fit to 400 m ($z = -H_{\text{top}} = -400$ m). The fitted temperature is given by

$$\hat{T}(z) = \frac{(T_0 - T_{-d})\left[1 + (d/A)^{2B}\right]}{(d/A)^{2B}\left[1 + (-z/A)^{2B}\right]} + T_{-d} - \frac{(T_0 - T_{-d})}{(d/A)^{2B}}, \quad 0 \geq z \geq -d, \tag{2.22a}$$

$$\hat{T}(z) = (T_{-H_{\text{TOP}}} T_{-d}) x^{ax+b} + T_{-d}, x \equiv -\frac{z+d}{H_{TOP} - d}, \quad -d \leq z \leq -H_{\text{TOP}}, \tag{2.22b}$$

where $T_0$ is SST. $T_{-d}$ is the temperature at the base of the seasonal thermocline $z = -d$. $T_{-H_{\text{TOP}}}$ is the temperature at the depth $H_{\text{TOP}}$ (400 m). Each temperature profile in the top layer (0–400 m depths) is represented by a set of eight parameters,

$$(T_0, T_{-d}, T_{-H_{\text{TOP}}}, d, A, B, a, b).$$

### 2.6.2 Mid-Depth Sub-Model (200–2,450 m)

An orthogonal polynomial expansion,

$$\hat{F}(D) = a_0 + a_1 P_{N1}(D) + \cdots + a_M P_{NM}(D) \tag{2.23}$$

is used to fit observed temperature and salinity profiles ($F$) for the depth range 200–2,450 m and salinity profiles over the range of 0–400 m (top submodel salinity profile). Here, $D$ represents the depth index; $D = 1, 2, \ldots, N$ for evenly spaced data in the layer. The polynomials, $P_{NK}(D)$, $K = 1, 2, \ldots, M$, are orthogonal Gram polynomials (Wylie 1975) defined by

$$P_{NK}(D) = \sum_{I=0}^{K} (-1)^I C_K^I C_{K+I}^I \frac{D^I}{N^I}. \tag{2.24}$$

The benefit of using orthogonal polynomial expansions is that computation of higher-order coefficients does not require re-computation of the lower-order coefficients. Each temperature (or salinity) profile is represented by a set of parameters, $(a_0, a_1, \ldots, a_M)$. In GDEM, $M = 6.0$ the maximum allowed rms error of fit is 0.1 ppt for the top salinity model, 0.05 ppt for the mid-depth salinity model, and 0.25°C for the mid-depth temperature model.

### 2.6.3 Deep Sub-Model (2,000 m to Bottom)

Deep temperature and salinity profiles are least squares fitted to a simple quadratic polynomial,

$$\hat{F}(z) = b_0 + b_1 z + b_2 z^2, \tag{2.25}$$

with rms errors less than 0.25°C for temperature and 0.05 ppt for salinity. The thermohaline parametric models (2.2), (2.17), and curve-fitting model (2.22)–(2.25) transform observed profiles with different data points in vertical into a set parameters. For example, the non-polar thermal parametric model (2.2) has 12 parameters with SST, five depths ($d_1$, $d_2$, $d_3$, $d_4$, $d_5$), and six gradients ($G_T^{(\mathrm{m})}, G_T^{(\mathrm{th})}, \bar{G}_T^{(\mathrm{en})}, \bar{G}_T^{(\mathrm{tr})}, \bar{G}_T^{(d1)}, \bar{G}_T^{(d2)}$). Since winter (December through April) profiles reveal a single-layer structure (Fig. 2.7a), the set of characteristic parameters reduces to (SST, $H$). The curve-fitting model has eight parameters in the shallow top sub-model, seven parameters in the mid-depth sub-model, and three parameters in the deep sub-model. The temperature and salinity profiles with irregular vertical sampling space can be represented by parameters with same number of data points. Furthermore, these parameters represent important physical features.

The non-polar parametric model (2.2) is used to process 4.5 million temperature profiles (Levitus and Boyer 1994) from NODC. Here, we present global (60°S–60°N) MLD ($d_1$) data for illustration. It is noted that the density depends non-linearly on temperature, salinity, and pressure. The MLD for density ($\mathrm{MLD}_\rho$) might not be the same as the MLD for temperature ($\mathrm{MLD}_T$).

## 2.7 Mixed Layer Depth

Two kinds of methods are used to determine the MLD: simple criteria and parametric modeling. The former were used by many oceanographers, and the later emerges after the parametric model was proposed (Chu et al. 1997b). Sections 2.4 and 2.5 describe the parametric models to determine the thermohaline parameters including the MLD. Here, we only present the simple criteria.

### 2.7.1 Simple Criteria

There are two types of criteria, difference and gradient, for determining $H_T$ and $H_D$ in the upper ocean. The difference criterion requires that the value for deviation of temperature (density) from its surface need to be smaller than a certain fixed value. The gradient criterion requires the vertical derivative of temperature (density) to be smaller than a certain fixed value.

The criterion for determining $\mathrm{MLD}_T$ varies from 0.5°C (Wyrtki 1961a,b; Monterey and Levitus 1997) to 0.8°C (Kara et al. 2000). The criterion for

determining $\mathrm{MLD}_\rho$ from potential density ($\sigma_\mathrm{t}$) profile is given by (Miller 1976; Spall 1991),

$$\Delta\sigma_\mathrm{t} = 0.125\sigma_\mathrm{t}(0), \tag{2.26a}$$

or by (Sprintall and Tomczak 1992; Ohlmann et al. 1996; Monterey and Levitus 1997),

$$\Delta\sigma_\mathrm{t} = 0.5^\circ\mathrm{C}\,(\partial\sigma_\mathrm{t}/\partial T). \tag{2.26b}$$

Here, $\partial\sigma_\mathrm{t}/\partial T$ is the thermal expansion coefficient evaluated using the surface values of temperature and salinity. The difference in criterion (2.26b) is based on the assumptions that the salinity effect on the seawater expansion is negligible, and that $\mathrm{MLD}_\rho$ is corresponding to the depth with temperature difference of 0.5°C from the surface (Sprintall and Tomczak 1992).

Defant (1961) was among the first to use the gradient method. He used a gradient of $0.015^\circ\mathrm{C\,m^{-1}}$ to determine $H_T$ of the Atlantic Ocean. Bathen (1972) chose $0.02^\circ\mathrm{C\,m^{-1}}$, and Lukas and Lindstrom (1991) used $0.025^\circ\mathrm{C\,m^{-1}}$. The following gradient criterion is widely used (e.g., Lukas and Lindstrom 1991)

$$\partial\sigma_\mathrm{t}/\partial z = 0.01\,\mathrm{kg\,m^{-4}}. \tag{2.26c}$$

### 2.7.2 $\mathrm{MLD}_T$

$\mathrm{MLD}_T$ is obtained from the MOODS data using the parametric model. The global (60°S–60°N) ocean is divided into 10° latitude by longitude boxes. Means and standard deviations are calculated for each box. Each $\mathrm{MLD}_T$ data point in the box is checked against the statistics. Any MLD data whose value exceeds three times the standard deviation is flagged out. Such a check is only performed if there are more than five or more MLD data points in the box. After the first check, means and standard deviations are re-calculated, excluding individual values which failed the first check. Such a procedure is repeated three times.

After the standard deviation check, we built up a raw $\mathrm{MLD}_T$ data set which contains 3.5 million data points. The data are unevenly distributed in space and time. Certain periods and areas are over sampled while others lack enough observations to gain any meaningful insights. Both North Pacific Ocean and North Atlantic Ocean, especially the Gulf Stream and Kuroshio, are featured as dense sampled regions. But, the Southern Hemispheric oceans are featured as low sampled regions. Quite a few areas have no $\mathrm{MLD}_T$ data both in January (Fig. 2.15a) and July (Fig. 2.15b) especially in the Southern Hemisphere. The temporally uneven distribution can be seen from Fig. 2.16, which indicates yearly number of temperature observations during 1958–1992 for the global oceans (Fig. 2.16). The year of 1966 is found to have the maximum number of profiles (around 120,000 profiles in the global oceans), and the year of 1992 is found to have the minimum number of profiles (near 10,000 profiles in the global oceans).

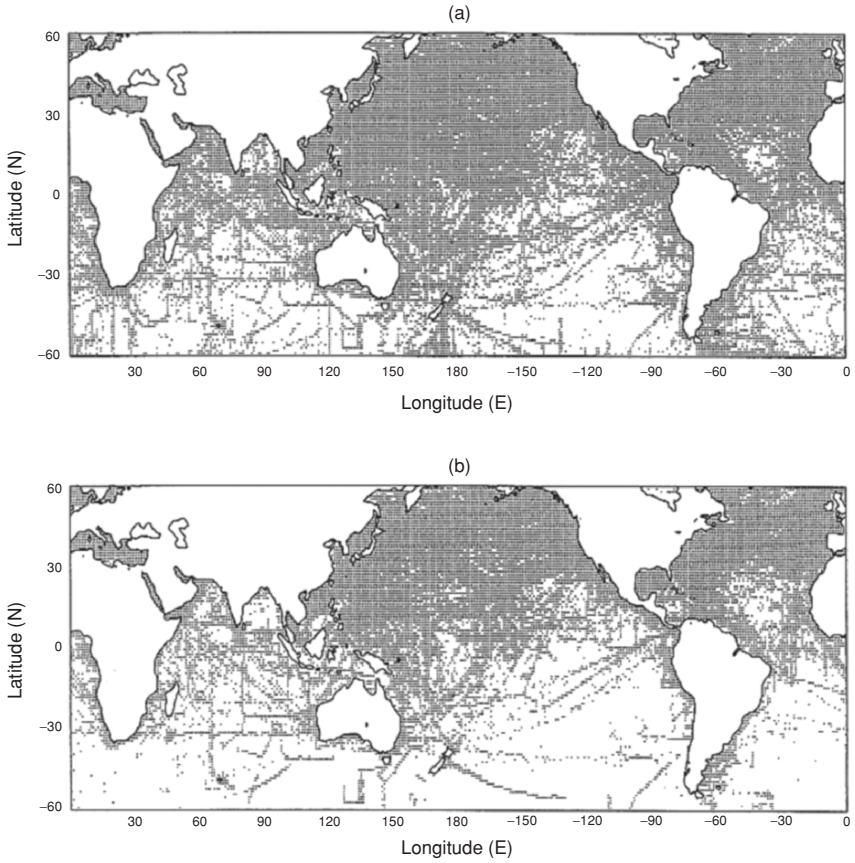


**Fig. 2.15.** $\mathrm{MLD}_T$ data distribution for the world oceans between 60°S and 60°N: (**a**) January, and (**b**) July (From Chu and Liu 1999, Proceedings on the 10th Symposium on Global Change Studies, American Meteorological Society)

The monthly mean gridded $\mathrm{MLD}_T$ data set is established using the optimal interpolation on $1^\circ \times 1^\circ$ grid points. Let $\mathrm{MLD}_T$ data be represented by $H_T(x_i, y_j, \tau_k, t_l)$, where, $\tau_k = 1958, 1959, \ldots, 1992$, is the time sequence in years, and $t_l = 1, 2, \ldots, 12$, the time sequence of month within a year. Before investigating the monthly variation of $\mathrm{MLD}_T$, two temporally averaging operators are defined,

$$\bar{H}_T(x_i, y_j, t_l) = \frac{1}{\Delta\tau} \sum_{k=1958}^{1992} H_T(x_i, y_j, \tau_k, t_l), \quad \Delta\tau = 35\,\mathrm{yr}, \tag{2.27a}$$

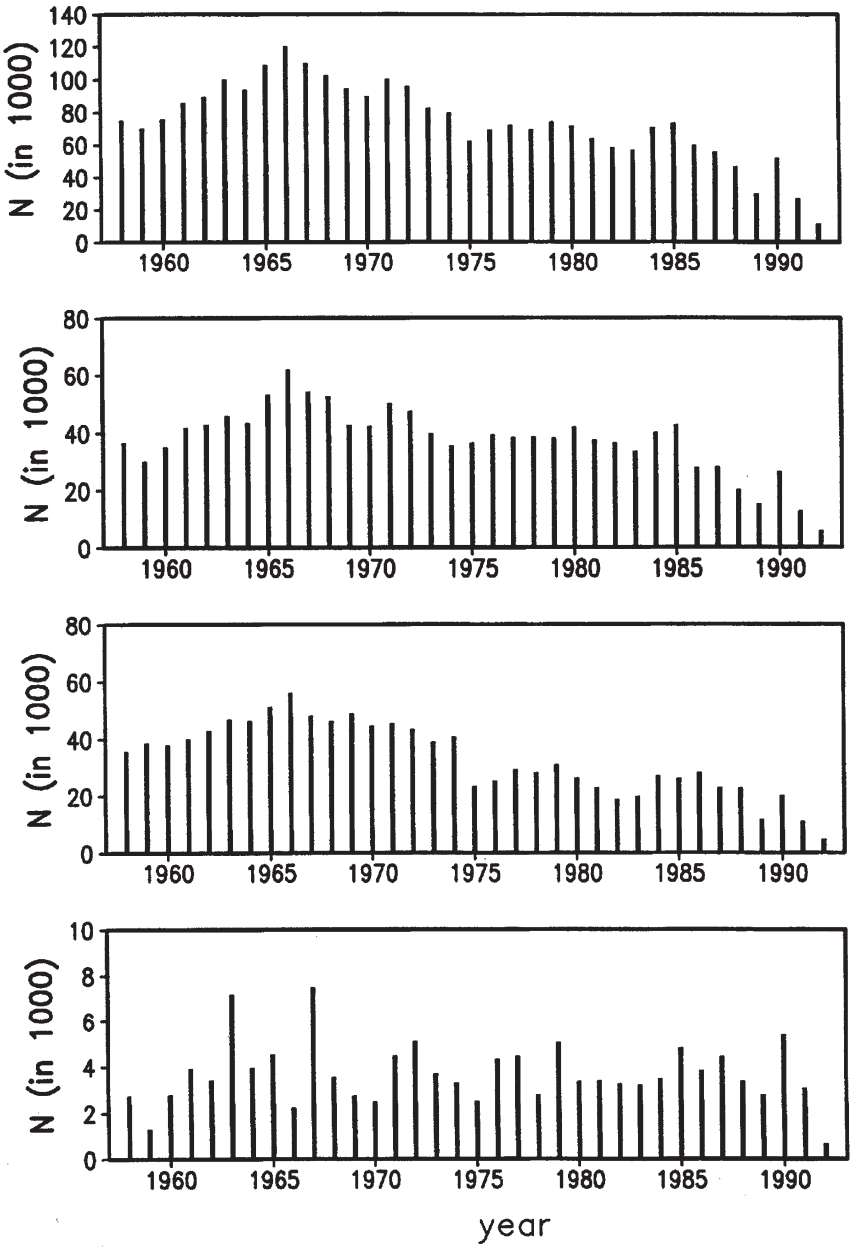


**Fig. 2.16.** Temporal variability of $\mathrm{MLD}_T$ data points of the world oceans (From Chu and Liu 1999, Proceedings on the 10th Symposium on Global Change Studies, American Meteorological Society)

which is the long-term mean value for the month $t_l$ (or called climatological monthly mean) and

$$\bar{\bar{H}}_T(x_i, y_j) = \frac{1}{12} \sum_{l=1}^{12} \bar{H}_T(x_i, y_j), \tag{2.27b}$$

which is the climatological annual mean.

It is noted that the $\mathrm{MLD}_T$ climatology (i.e., climatological monthly and/or annual mean) computed here is different from the $\mathrm{MLD}_T$ climatology calculated from the monthly mean temperature profiles (Monterey and Levitus 1997). The $\mathrm{MLD}_T$ climatology is quite different between the two approaches because the spatial average of $\mathrm{MLD}_T$ from observed temperature profiles (first approach) is different from the $\mathrm{MLD}_T$ of the spatially averaged temperature profiles over that data set (second approach). Usually, the $\mathrm{MLD}_T$ calculated using the second approach is much thicker than the one using the first approach.

Monthly mean $\mathrm{MLD}_T$ (Fig. 2.17) show several interesting features: (a) deep mixed layer ($\mathrm{MLD}_T \geq 60\,\mathrm{m}$) in the northeast part of the North Atlantic Ocean, (b) zonally asymmetric pattern in the tropical Pacific with deep $\mathrm{MLD}_T$ ($\geq 40\,\mathrm{m}$) in the western part, and shallow $\mathrm{MLD}_T$ ($\leq 20\,\mathrm{m}$) in the eastern part.

Different characteristics of the El Nino-Southern Oscillation (ENSO) between the 1980s duration and the 1960s and 1970s durations lead to the investigation of connection between SST inter-annual and inter-decadal variabilities. The connection should also be identified using the $\mathrm{MLD}_T$ data. To do so, the seasonal variability should be filtered out, and the $\mathrm{MLD}_T$ anomaly to the climatological monthly mean is calculated

$$\hat{H}_T(x_i, y_j, \tau_k, t_l) = H_T(x_i, y_j, \tau_k, t_l) - \bar{H}_T(x_i, y_j, t_l). \tag{2.28}$$

Since the data $\hat{H}_T(x_i, y_j, \tau_k, t_l)$ are not sufficient to obtain statistically significant results on $1^\circ \times 1^\circ$ grid, the latitudinally averaged (10°S–10°N) anomalies for the Pacific Ocean and zonally averaged anomalies for the Pacific and Atlantic Oceans are calculated. The inter-annual variability can be identified from latitudinally averaged $\mathrm{MLD}_T$ anomaly in the equatorial Pacific. Time-longitude plot of $\mathrm{MLD}_T$ anomaly from January 1958 to December 1992 (Fig. 2.18) shows westward propagated equatorial Rossby waves and eastward propagated equatorial Kelvin waves. Most negative $\mathrm{MLD}_T$ anomalies propagate westward from the eastern Pacific with speeds from 25 to $10\,\mathrm{cm\,s^{-1}}$. The westward propagating events with maximum negative anomaly ($-10\,\mathrm{m}$) are identified during 1959–1960, 1971–1974, 1981–1985, and 1988–1992. It takes 2–5 years across the basin. This indicates that the mixed layer shallows as the equatorial Rossby waves propagate. This confirms the results from earlier numerical mode simulations (McCreary and Anderson 1984). The decadal variability can be identified from zonal averaged MLD anomaly in the Pacific and Atlantic Oceans from time-latitude plot of $\mathrm{MLD}_T$ anomaly from January 1958 to December 1992 (Fig. 2.19).

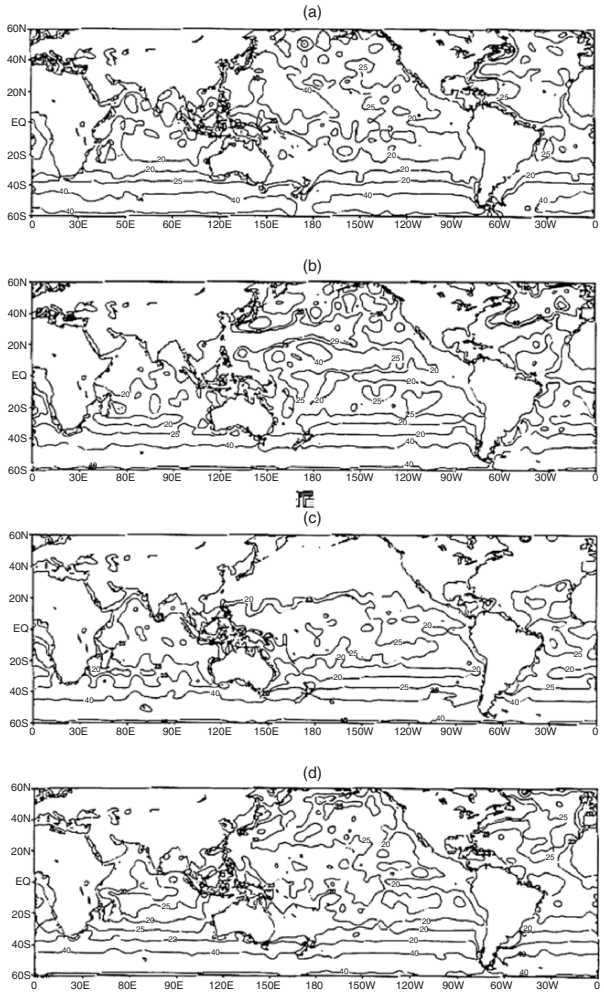


**Fig. 2.17.** Climatological monthly mean $\mathrm{MLD}_T$: (**a**) January, (**b**) April, (**c**) July, and (**d**) October (From Chu and Liu 1999, Proceedings on the 10th Symposium on Global Change Studies, American Meteorological Society)

## 2.8 Barrier Layer

There are areas of the world ocean where $\mathrm{MLD}_T$ (represented by $H_T$) is larger than $\mathrm{MLD}\rho$ (represented by $H_D$) (Lindstrom et al. 1987; Lukas and Lindstrom 1991; Sprintall and Tomczak 1992; You 1995, 1998; Chu et al. 2001d). When the "barrier layer" occurs ($H_T > H_D$), the barrier layer thickness is defined as the difference, $H_T$–$H_D$ (Fig. 2.20). There is a little temperature change (near-zero vertical gradient) and a great density change in the barrier layer, which isolates the density mixed layer from the cool water below

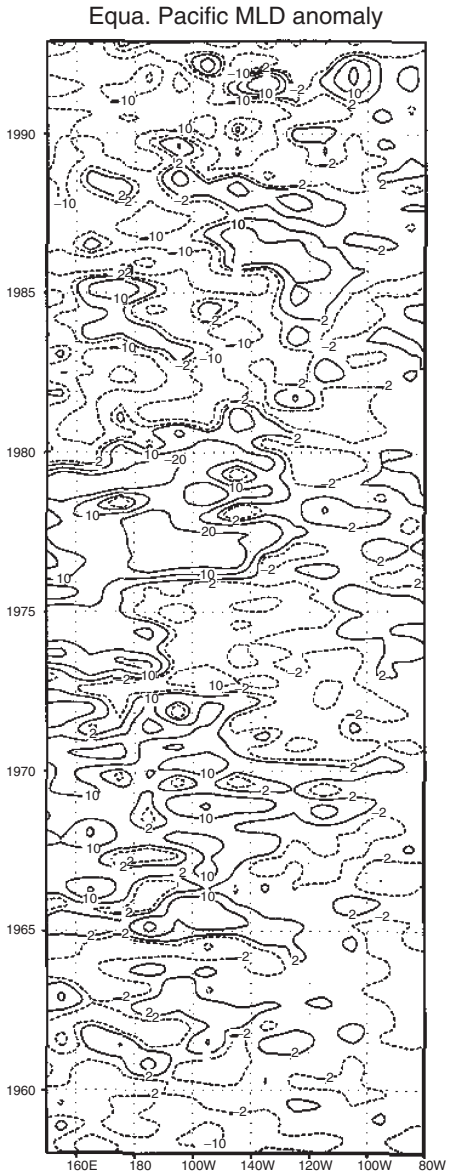


**Fig. 2.18.** Time-longitude plot of monthly $\mathrm{MLD}_T$ anomaly in the equatorial Pacific averaged between 10°S and 10°N (From Chu and Liu 1999, Proceedings on the 10th Symposium on Global Change Studies, American Meteorological Society)

the thermal mixed layer (i.e., the thermocline). Such insolation makes SST vary in a short period when the net surface heat flux is not negligible, which has impacts on ocean heat budgets (Swenson and Hansen 1999) and affects

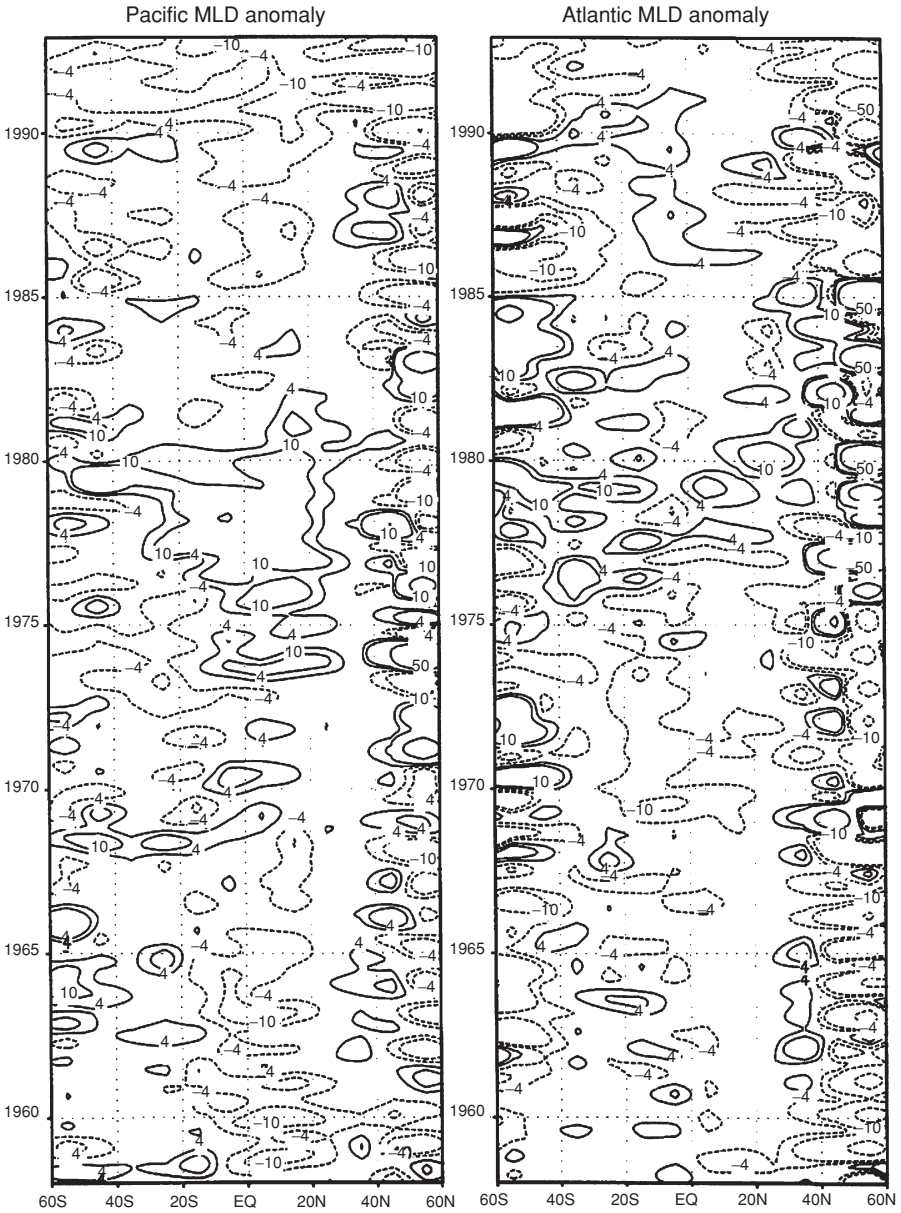


**Fig. 2.19.** Time-latitudinal plot of zonally averaged monthly $\mathrm{MLD}_T$ anomaly in the (**a**) Pacific Ocean, and (**b**) Atlantic Ocean (From Chu and Liu 1999, Proceedings on the 10th Symposium on Global Change Studies, American Meteorological Society)

the heat exchange with the atmosphere. Therefore, understanding spatial and temporal distributions of a barrier layer leads to accurate estimate of upper ocean thermohaline structure and the air–ocean fluxes.

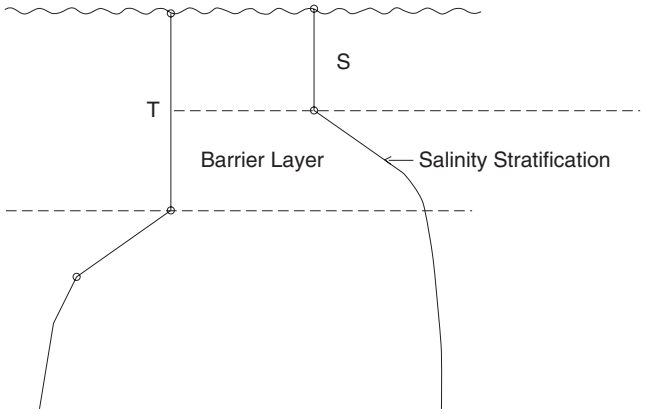


**Fig. 2.20.** A sketch diagram of isothermal, mixed, and barrier layers (from Chu et al. 2001d, Journal of Physical Oceanography)

Barrier layer occurs in open oceans and regional seas. Identification of the barrier layer can be conducted after analyzing the hydrographic data. For example, Chu et al. (2001d) identify the occurrence of barrier layer in the Sulu and Celebes Seas from the CTD data of the MOODS data.

### 2.8.1 Two Mechanisms for the Occurrence of Barrier Layer

Two major factors determining $H_T(H_D)$ are: (1) surface winds and net heat (buoyancy) flux and (2) thermal (density) stratification underneath the isothermal (mixed) layer. Thus, the condition ($H_T > H_D$) is caused by the surface fresh water flux (precipitation excess evaporation) and strong salinity stratification underneath the mixed layer. Thus, the barrier layer can be classified as (a) rain-formed, and (b) stratification-formed (weaker thermal and strong salinity stratification).

There are two regimes in the ocean mixed layer dynamics (Chu 1988; Chu et al. 1990; Chu and Garwood 1990, 1991; Chu 1993): entrainment and detrainment. The detrainment process occurs with weak winds, and strong surface warming (or excessive precipitation over evaporation). The two depths $H_T$ and $H_D$ are determined by

$$H_T = \frac{C_1 u_*^3}{C_2 \alpha_* g F/\rho_0 c_p}, \quad H_D = \frac{C_1 u_*^3}{C_2 B}, \tag{2.29}$$

where $C_1$ and $C_2$ are tuning coefficients, $g$ the gravity, $\alpha_*$ the thermal expansion coefficient, $\rho_0$ the characteristic density, $c_p$ the specific heat under constant pressure, $F$ the net surface heat flux (downward positive). In detrainment regime, we have $F > 0$. The ratio between the two depths is calculated by

$$\frac{H_T}{H_D} = 1 + \frac{\beta_*(P-E)S}{\alpha_* F/\rho_0 c_p}, \tag{2.30}$$

where $P$ and $E$ are the precipitation and surface evaporation rate, and $\beta_*$ is the salinity contraction coefficient. Thus, the rain-formed mechanism ($P$–$E > 0$) becomes evident in the detrainment regime with weak winds, weak surface warming (low positive value of $F$), and strong surface fresh water flux [(large positive value of $(P$–$E)$].

The stratification-formed mechanism is evident in the entrainment regime. Suppose that the rain-formed mechanism is absent ($P = E$) and that the initial $H_T$ coincides with $H_D$,

$$H_T\,|_{t=0} = H_D\,|_{t=0}. \tag{2.31}$$

The ratio of the initial entrainment velocities ($w_\mathrm{e} = \mathrm{d}H/\mathrm{d}t$) between isothermal and mixed layers is given by (Chu 1993)

$$\frac{w_\mathrm{e}^{(T)}}{w_\mathrm{e}^{(D)}} = \frac{[-(\rho - \rho_{-H_D})]}{\alpha_*(T - T_{-H_T})}. \tag{2.32}$$

A larger density jump

$$[-(\rho - \rho_{-H_D})] > \alpha_*(T - T_{-H_T}) \tag{2.33}$$

causes a larger entrainment velocity for the mixed thermal layer than the mixed density layer. Since the density stratification is determined by the temperature and salinity stratifications, the stratification-formed mechanism becomes important when the salinity stratification is strong. Thus, the stratification-formed mechanism becomes evident in the entrainment regime with strong winds, strong surface cooling (negative value of $F$), and strong salinity stratification. Usually, both rain-formed and stratification-formed mechanisms may take place at the same time; and precipitation may also strengthen the stratification.

### 2.8.2 Sulu and Celebes Seas

The Sulu and Celebes Seas are the two major marginal seas in the outer southeastern Asia region (Fig. 2.21), which consists of an island arc stretching across some 5,150 km along the equator at about 94°E–14°E and 15°N–11°S, and which has two contrasting zones (Arief 1998). The Sulu Sea belongs to the western zone where approximately 15–20% of the global freshwater discharge enters (Toole 1987) from freshwater influx that is supported by a high annual rainfall, between 2 and 4 $\mathrm{m\,y^{-1}}$, (ASEAN Subcommittee on Climatology 1982). The Celebes Sea belongs to the eastern zone which is composed of deep-basin chains of 1,000–4,000 m depth and filled mainly by western Pacific water masses. This zone has a low annual rainfall, less than 2 $\mathrm{m\,y^{-1}}$ (ASEAN Subcommittee on Climatology 1982).

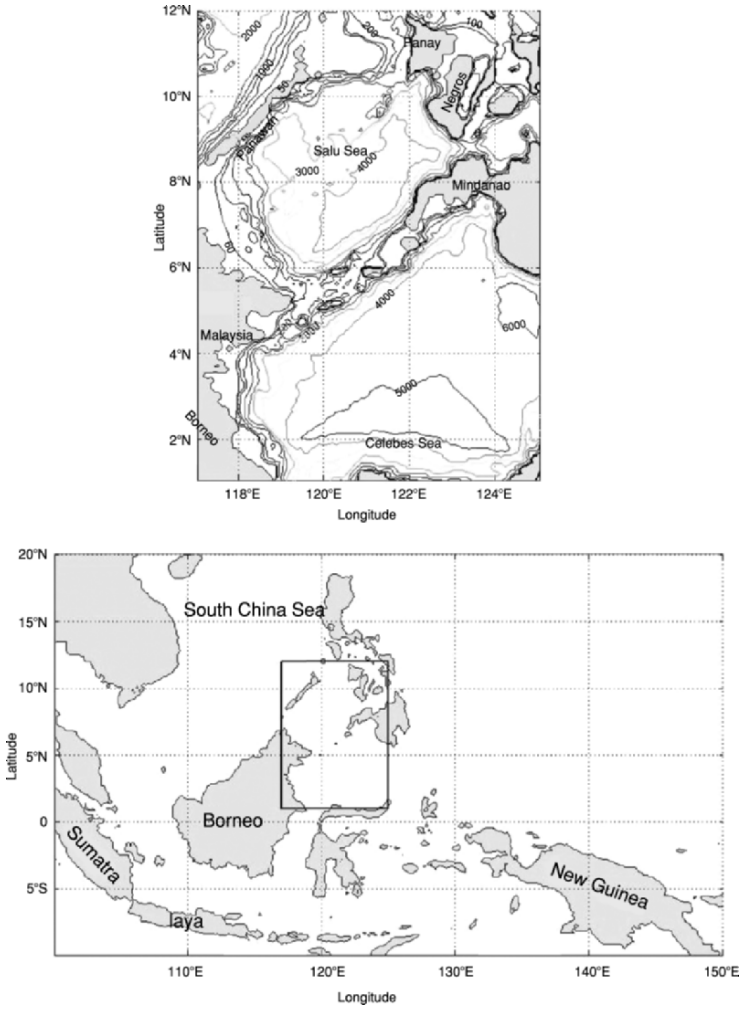


**Fig. 2.21.** Geography and isobaths showing the bottom topography of the Sulu and Celebes Seas (from Chu et al. 2001d, Journal of Physical Oceanography)

### 2.8.3 Barrier Layer in the Sulu Sea

The two depths, $H_T$ and $H_D$, are obtained from 221 CTD profiles. Monthly CTD stations (denoted by the symbol "o") and the stations with the barrier layer occurrence ($H_T > H_D$, represented by the symbol "+") in the Sulu Sea (Fig. 2.22) show a rather frequent occurrence of barrier layer. For example, among 16 (6) CTD stations in September (November), there are 15 (6) stations where the barrier layer occurs. The rate of occurrence reaches 94% in September and 100% in November (Table 2.1). When barrier layer occurs, the barrier layer thickness is computed as the difference between $H_T$ and $H_D$. The

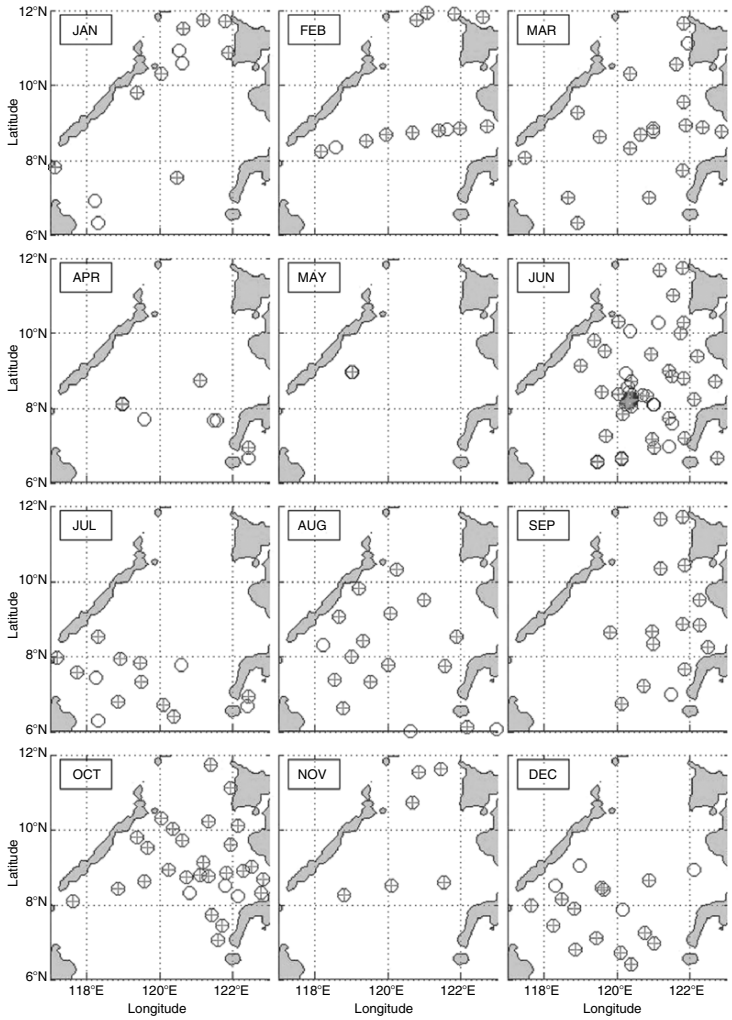


**Fig. 2.22.** Monthly CTD stations (denoted by the symbol "o") and the stations with the barrier layer occurrence ($H_T > H_D$, represented by the symbol "+") in the Sulu Sea (after Chu et al. 2001d, Journal of Physical Oceanography)

climatological characteristics are outlined as follows: (a) barrier layer occurs most frequent in September–November (fall) with a frequency of 90–100% and least frequent in April and May (spring) with a frequency of 50%; (b) MLD has a minimum value of 3 m in May and a maximum value of 30.5 m in February; and (c) barrier layer depth has large values (39.7–47.6 m) in September–October and small values (9–11.3 m) in April and May. It is noted that the sample size is not sufficiently large, thus the statistical features mentioned here may have bias values, especially in May.

**Table 2.1.** Monthly occurrence frequency and climate features of the barrier layer in the Sulu Sea

| | Jan | Feb | Mar | Apr | May | Jun | Jul | Aug | Sep | Oct | Nov | Dec |
|---|---|---|---|---|---|---|---|---|---|---|---|---|
| N | 12 | 13 | 19 | 8 | 2 | 61 | 16 | 19 | 16 | 31 | 6 | 18 |
| B | 8 | 11 | 17 | 4 | 1 | 48 | 11 | 16 | 15 | 28 | 6 | 14 |
| B/N (%) | 67 | 85 | 89 | 50 | 50 | 79 | 69 | 84 | 94 | 90 | 100 | 78 |
| mean MLD (m) | 29 | 30.5 | 19.5 | 16.5 | 3 | 16.4 | 14.2 | 12.9 | 11.1 | 14.9 | 21.2 | 12.1 |
| mean barrier layer thick-ness (m) | 27.5 | 29.9 | 14.1 | 11.3 | 9.0 | 12.2 | 28.7 | 29.3 | 39.7 | 47.6 | 33.7 | 45.3 |

$N$ is the number of station, and $B$ is the number of barrier layer occurrence (after Chu et al. 2001d, Journal of Physical Oceanography)

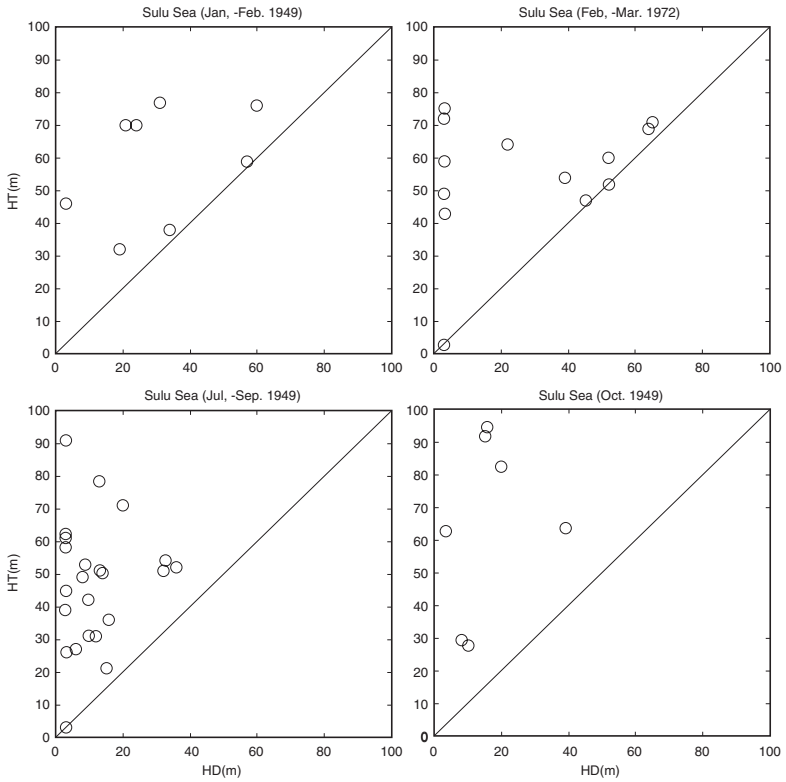


**Fig. 2.23.** Scatter diagrams ($H_T$ versus $H_D$) of the Sulu Sea for the four selected periods: (**a**) January–February 1949, (**b**) February–March 1972, (**c**) July–September 1949, and (**d**) October–December 1973 (after Chu et al. 2001d, Journal of Physical Oceanography)

Scatter diagrams of $H_T$ and $H_D$ (Fig. 2.23) show that the barrier layer occurs quite often in both summer and winter, with more evidence in the summer months. For example, $H_D$ is lesser than $H_T$ at almost all stations

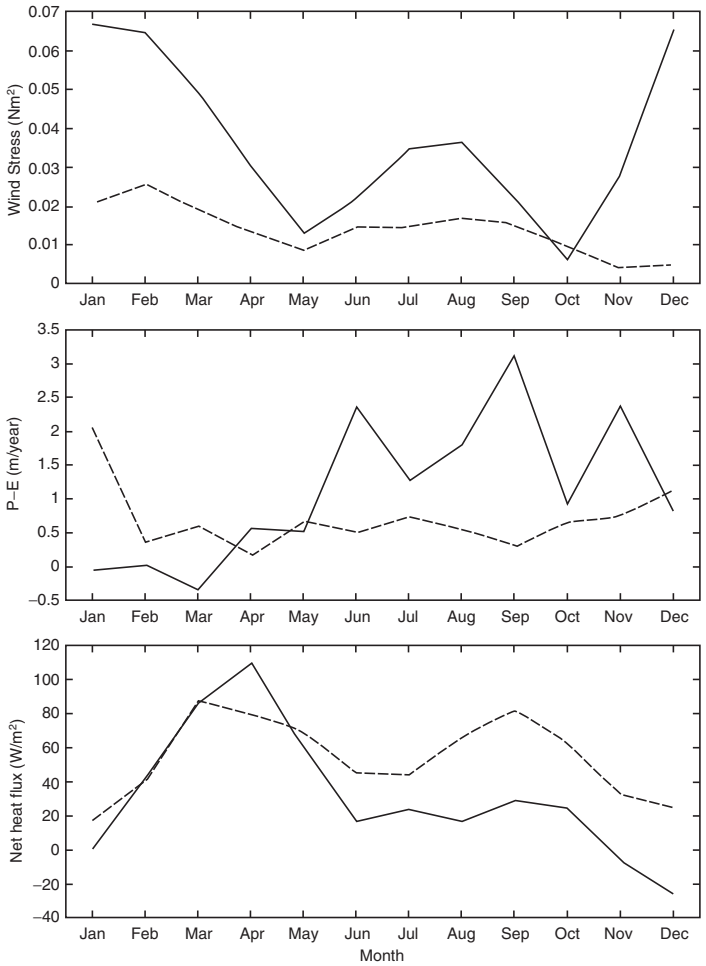


**Fig. 2.24.** Monthly mean COADS (**a**) surface wind stress ($\mathrm{N\,m^{-2}}$), (**b**) $P$–$E$ ($\mathrm{m\,yr^{-1}}$), and (**c**) net heat flux ($\mathrm{W\,m^{-2}}$) averaged over the Sulu Sea (solid curve) and the Celebes Sea (*dashed curve*) (after Chu et al. 2001d, Journal of Physical Oceanography)

in October 1973. Comparing among the four periods, the barrier layer has relatively thin barrier layer in July–September 1949.

The Comprehensive Ocean-Atmosphere Data Set (COADS) provides monthly mean sea surface wind stress and net heat and freshwater fluxes (Fig. 2.24). The surface wind stress, net heat flux ($F$), and net fresh water flux ($P$–$E$) have seasonal variability in the Sulu Sea. The wind stress strengthens in December–February ($6.57$–$6.67 \times 10^{-2}\,\mathrm{N\,m^{-2}}$) and weakens in April–November ($0.63$–$3.66 \times 10^{-2}\,\mathrm{N\,m^{-2}}$). The net heat flux is negative in November–January ($-25.4$ to $0\,\mathrm{W\,m^{-2}}$, surface cooling) and becomes largely

positive in March–May (60–110.3 $\mathrm{W\,m^{-2}}$, strong surface warming). The surface fresh water flux ($P-E$) is weak in January–May ($<$0.6 $\mathrm{m\,yr^{-1}}$) and strong in June–November ($>$1 $\mathrm{m\,yr^{-1}}$).

In April and May the Sulu Sea is under the influence of weak winds (1.3–3 $\times 10^{-2}\,\mathrm{N\,m^{-2}}$), strong net heat flux (60–110.3 $\mathrm{W\,m^{-2}}$), and weak surface fresh water flux (0.52–0.56 $\mathrm{m\,yr^{-1}}$). The strong heat flux and weak winds cause shallow isothermal layer (small $H_T$). The weak fresh water flux cannot strengthen the salinity stratification. Thus, the frequency of the barrier layer is the least in April and May. In September and October the Sulu Sea is under the influence of weak winds (0.63–2.19 $\times 10^{-2}\,\mathrm{N\,m^{-2}}$), weak net heat flux (24.6–29.2 $\mathrm{W\,m^{-2}}$), and strong surface fresh water flux (3.1 $\mathrm{m\,yr^{-1}}$ in September). These conditions lead to the detrainment regime for the upper ocean and favor the rain-formed mechanism (excessive precipitation over evaporation).

In December the Sulu Sea is under the influence of strong winds (6.57 $\times$ $10^{-2}\,\mathrm{N\,m^{-2}}$), surface cooling ($-25.4\,\mathrm{W\,m^{-2}}$), and relatively weak surface fresh water flux (0.8 $\mathrm{m\,yr^{-1}}$). These conditions favor the entrainment regime in the upper ocean and the stratification-formed mechanism for the occurrence of barrier layer.

### 2.8.4 Barrier Layer in the Celebes Sea

The two depths ($H_T$ and $H_D$) for the Celebes Sea are obtained from processing 179 CTD profiles. Monthly CTD stations (denoted by the symbol "o") and the stations with the barrier layer occurrence ($H_D < H_T$, represented by the symbol "+") in the Celebes Sea (Fig. 2.25) show a rather frequent occurrence of barrier layer in the Celebes Sea. For example, among 14 CTD stations in December, there are 13 stations where barrier layer occurs. The rate of occurrence reaches 93% (Table 2.2). The barrier layer thickness has a maximum value of 62.0 m in April and a minimum value of 9.6 m in June. The climatological features of barrier layer are outlined as follows: (a) barrier layer occurs most frequent in December with a frequency of 93% and least frequent in April with a frequency of 36%; (b) MLD has a minimum value of 7.3 m in March and a maximum value of 28.1 m in September; and (c) barrier layer thickness has a maximum value in March–April (49.7–62.0 m) and a minimum value of 9.6 m in June. These numbers might not have statistical significance due to the size of the sample being small.

Scatter diagrams of $H_T$ and $H_D$ (Fig. 2.26) show that the barrier layer occurs quite often in winter and fall and less often in spring. For example, $H_D$ is lesser than $H_T$ at almost all stations in January 1941. At Station 16, $H_D$ and $H_T$ are 25 and 100 m, respectively with a barrier layer thickness of about 75 m. Among the four periods, the barrier layer has relatively thin barrier layer in July 1941 and May–June 1972.

The surface wind stress, net heat flux ($F$), and net fresh water flux ($P$–$E$) have less seasonal variability in the Celebes Sea than in the Sulu Sea (Fig. 2.24). The wind stress varies between 0.45 $\times 10^{-2}\,\mathrm{N\,m^{-2}}$ (November)

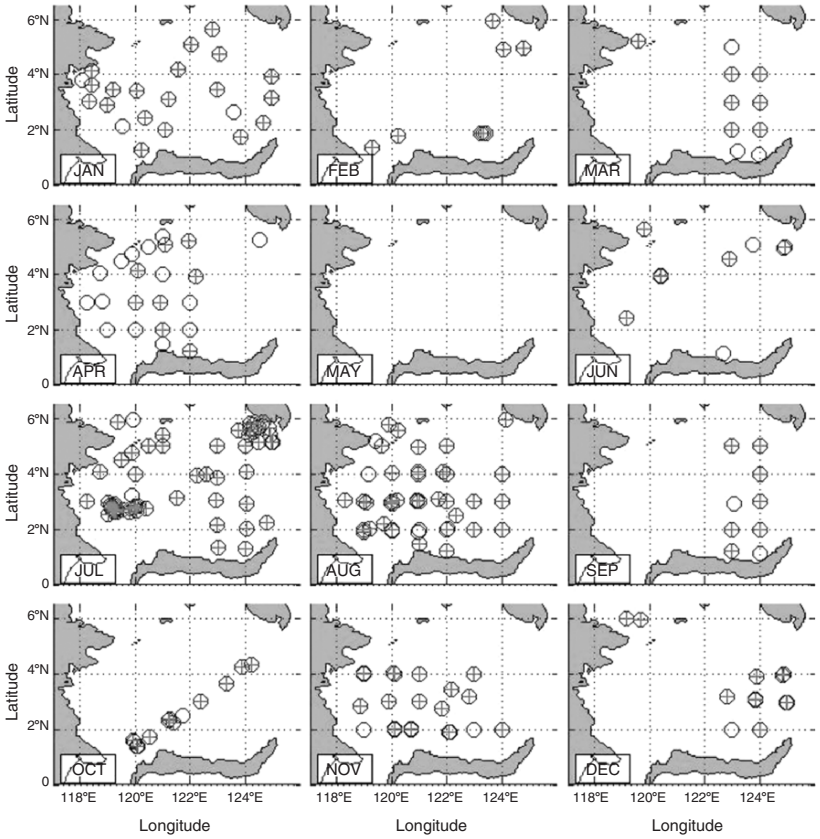


**Fig. 2.25.** Monthly CTD stations (denoted by the symbol "o") and the stations with the barrier layer occurrence ($H_D < H_T$, represented by the symbol "r") in the Celebes Sea (after Chu et al. 2001d, Journal of Physical Oceanography)

and $2.6 \times 10^{-2}\,\mathrm{N\,m^{-2}}$ (February). The surface net heat and fresh water fluxes are positive all year round with $F$ varying from $17.5\,\mathrm{W\,m^{-2}}$ (January) to $87.4\,\mathrm{W\,m^{-2}}$ (March) and $(P–E)$ varying from $0.17\,\mathrm{m\,yr^{-1}}$ (April) to $2.1\,\mathrm{m\,yr^{-1}}$ (January). Thus, the Celebes Sea is under the influence of weak winds, surface warming, and surface fresh water flux all year round. These conditions favor the rain-formed mechanism.

In December–January the Celebes Sea is experienced weak net heat flux (17.5–$24.5\,\mathrm{W\,m^{-2}}$), and strong surface fresh water flux (1.14–$2.06\,\mathrm{m\,yr^{-1}}$). These conditions may cause the detrainment regime for the upper ocean and favor the rain-formed mechanism (excessive precipitation over evaporation).

In April, the Celebes Sea experiences strong net heat flux ($80.4\,\mathrm{W\,m^{-2}}$), and weak surface fresh water flux ($0.17\,\mathrm{m\,yr^{-1}}$). The strong heat flux and weak winds cause shallow isothermal layer (small $H_T$). The weak fresh water flux

**Table 2.2.** Monthly occurrence frequency and climate features of the barrier layer in the Sulu Sea

| | Jan | Feb | Mar | Apr | May | Jun | Jul | Aug | Sep | Oct | Nov | Dec |
|---|---|---|---|---|---|---|---|---|---|---|---|---|
| B | 8 | 11 | 17 | 4 | 1 | 48 | 11 | 16 | 15 | 28 | 6 | 14 |
| N | 12 | 13 | 19 | 8 | 2 | 61 | 16 | 19 | 16 | 31 | 6 | 18 |
| B/N (%) | 67 | 85 | 89 | 50 | 50 | 79 | 69 | 84 | 94 | 90 | 100 | 78 |
| mean MLD (m) | 29 | 30.5 | 19.5 | 16.5 | 3 | 16.4 | 14.2 | 12.9 | 11.1 | 14.9 | 21.2 | 12.1 |
| mean barrier layer thick-ness (m) | 27.5 | 29.9 | 14.1 | 11.3 | 9.0 | 12.2 | 28.7 | 29.3 | 39.7 | 47.6 | 33.7 | 45.3 |

$N$ is the number of station, and $B$ is the number of barrier layer occurrence (after Chu et al. 2001d, Journal of Physical Oceanography)

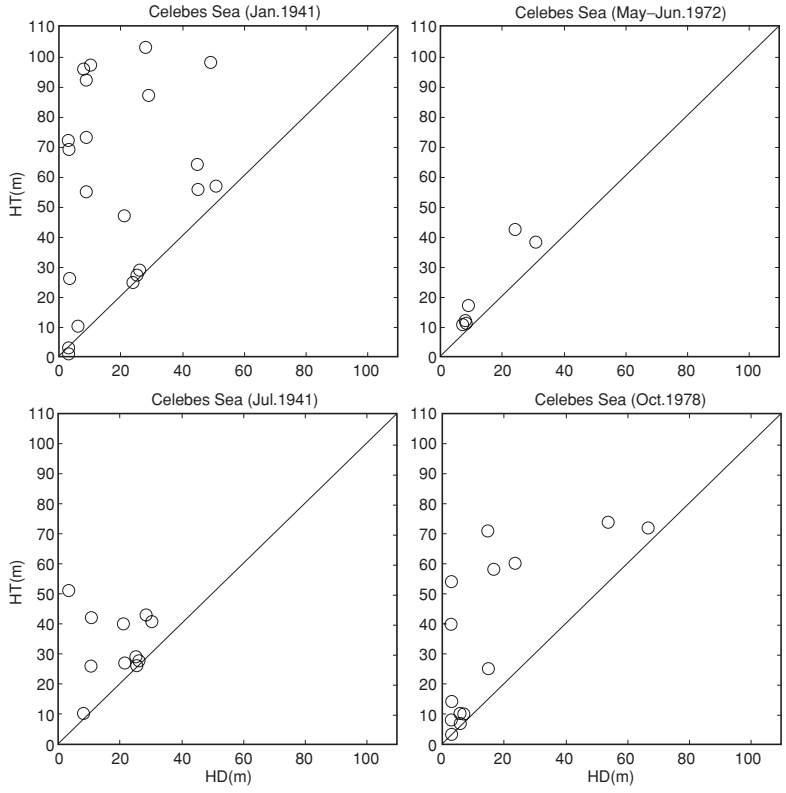


**Fig. 2.26.** Scatter diagrams ($H_T$ versus $H_D$) of the Celebes Sea for the four selected periods: (**a**) January–February 1949, (**b**) February–March 1972, (**c**) July–September 1949, and (**d**) October–December 1973 (after Chu et al. 2001d, Journal of Physical Oceanography)

strengthens the salinity stratification slightly. Thus, the barrier layer occurs least frequently in April.

## 2.9 Determination of Vertical Temperature Structure from SST

The most difficult problem in physical oceanography is the lack of in situ observations. With the help of electromagnetic techniques, especially satellite remote-sensing, we may obtain global coverage of temporally varying surface data such as SST. Can we determine the vertical thermal structure from satellite SST observations? To answer this question we should first examine the linkage between SST and sub-surface thermal structure (Fig. 2.27). The key issue is how to compress a large profile data set into a small parameter (or coefficient) data set. Parametric models (see Sects. 2.4 and 2.5) uses the layered structure (mixed layer, entrainment zone, thermocline or halocline, and deep layer) to transform the profile data into a set of physical parameters such as SST, $\mathrm{MLD}_T$, thermocline bottom depth, thermocline temperature gradient, and deep layer stratification (Chu et al. 2000a). Using parametric models depicted in Sects. 2.4 and 2.5, a vertical temperature profile can be transformed into several parameters: SST, $\mathrm{MLD}_T$, thermocline bottom depth, thermocline temperature gradient, and deep layer stratification.

These parameters vary on different time scales: SST and $\mathrm{MLD}_T$ on scales of minutes to hours, the thermocline bottom depth and thermocline temperature gradient on months to seasons, and deep layer stratification on an even longer time-scale. If the long time-scale parameters such as the thermocline bottom

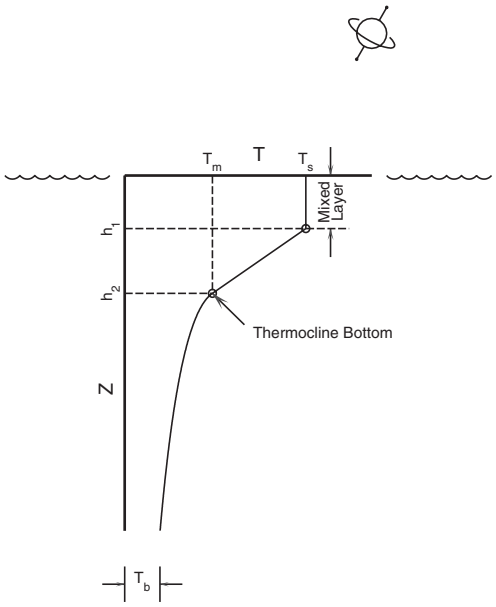


**Fig. 2.27.** SST and temperature profile (after Chu et al. 2000a, Journal of Atmospheric and Oceanic Technology)

depth, thermocline temperature gradient, and deep layer stratification are known (or given by climatological values), the degree of freedom of a vertical profile fitted by the model reduces to one: SST. When SST is observed, we may invert $\mathrm{MLD}_T$, and, in turn, the vertical temperature profile with the known longtime-scale parameters. Using the parametric model, the inversion of the sub-surface thermal structure from satellite SST becomes a relationship between SST and sub-surface parameters.

### 2.9.1 Methodology

Keeping the minimal possible degrees of freedom, the thermal parametric model (2.2a)–(2.2f) can be simply depicted by (see Fig. 2.27),

$$T(z) = T_\mathrm{S}, \quad (0 \geq z \geq h_1), \tag{2.34a}$$

$$T(z) = T_\mathrm{S} + G_\mathrm{th}(z + h_1), \quad (-h_1 \geq z \geq -h_2) \tag{2.34b}$$

$$T(z) = T_\mathrm{d} + (T_\mathrm{tb} - T_\mathrm{d}) \exp\left[\frac{z_0^\alpha - (z_0 - z - h_2)^\alpha}{H^\alpha}\right], \quad (z \leq -h_2), \tag{2.34c}$$

where $T_\mathrm{S}, T_\mathrm{tb}$, and $T_\mathrm{d}$ are SST, temperature at the thermocline bottom depth, and a deep temperature; $h_1, h_2, H$ are $\mathrm{MLD}_T$, thermocline bottom depth, and a lower layer e-folding scale, respectively; and $G_\mathrm{th}$ is thermocline temperature gradient. The deep temperature, $T_\mathrm{d}$, is the temperature at the deepest ocean depth such as 5,500 m in the climatological data (Levitus and Boyer 1994). For shallow water regions, $T_\mathrm{d}$ is, of course, not a real observed value but an extrapolated value to the deepest depth (e.g., 5,500 m). We use $T_\mathrm{d}$ to keep the data above the bathymetry, fitting the parametric model (2.34).

Here, the thermocline is featured by a linear profile (constant $G_\mathrm{th}$), and the lower layer is characterized by a non-linear profile. To guarantee $T(z)$ and $\mathrm{d}T(z)/\mathrm{d}z$ continuous at $z = -h_2$,

$$T(h_2 + 0) = T(h_2 - 0), \quad \frac{\mathrm{d}T(h_2 + 0)}{\mathrm{d}z} = \frac{\mathrm{d}T(h_2 - 0)}{\mathrm{d}z} = G_\mathrm{th} \tag{2.35}$$

determines the two additional parameters, $z_0$ and $a$. Differentiating (2.34) with respect to $z$ and using (2.35) yield

$$z_0 = \left[\frac{HG_\mathrm{th}}{a(T_\mathrm{tb} - T_\mathrm{d})}\right]^{1/(a-1)}. \tag{2.36}$$

The parameter $a$ cannot be zero nor be greater than or equal to one. Otherwise, $z_0$ becomes very large and distorts the e-folding decrease of temperature with depth. Chu et al. (2000a) use $a = 0.5$. Thus, from a vertical temperature profile we may extract three temperatures $(T_\mathrm{S}, T_\mathrm{tb}, T_\mathrm{d})$, three depths

$(h_1, h_2, H)$, and one gradient $G_{\rm th}$, seven parameters in total. We require continuity of temperature $z = -h_2$,

$$T_{\rm S} - G_{\rm th}(h_2 - h_1) = T_{\rm tb}. \tag{2.37}$$

Therefore, any six of the seven parameters $(T_{\rm S},\ T_{\rm tb},\ T_{\rm d}, h_1, h_2, H, G_{\rm th})$ determine a vertical profile. Thus, the degrees of freedom of the thermal parametric model are six.

### 2.9.2 Example – South China Sea

The South China Sea has bottom topography (Fig. 2.28) that makes it a unique semi-enclosed ocean basin that is seasonally forced by a pronounced monsoon surface wind. Extended continental shelves (less than 100 m deep) exist along the north boundary and across the southwest portion of the basin, while steep slopes with almost no shelf are found along the eastern boundary. The deepest water is confined to an oblate bowl oriented SW–NE, centered at 13°N. The maximum depth is around 4,500 m. The MOODS temperature profiles of the South China Sea are used for the analysis. After quality control, a subset is used consisting of May (1932–1994) 10,153 profiles (Fig. 2.29).

In May, for the years 1986–1994, there are 40 daytime Multi-Channel SST (MCSST) and MOODS data points which are co-located in the same week,

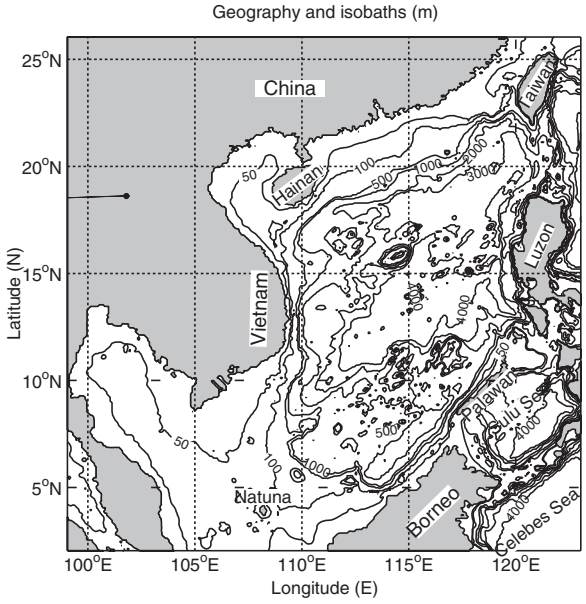


**Fig. 2.28.** Geography and isobaths showing the bottom topography of the South China Sea (from Chu et al. 2000a, Journal of Atmospheric and Oceanic Technology)

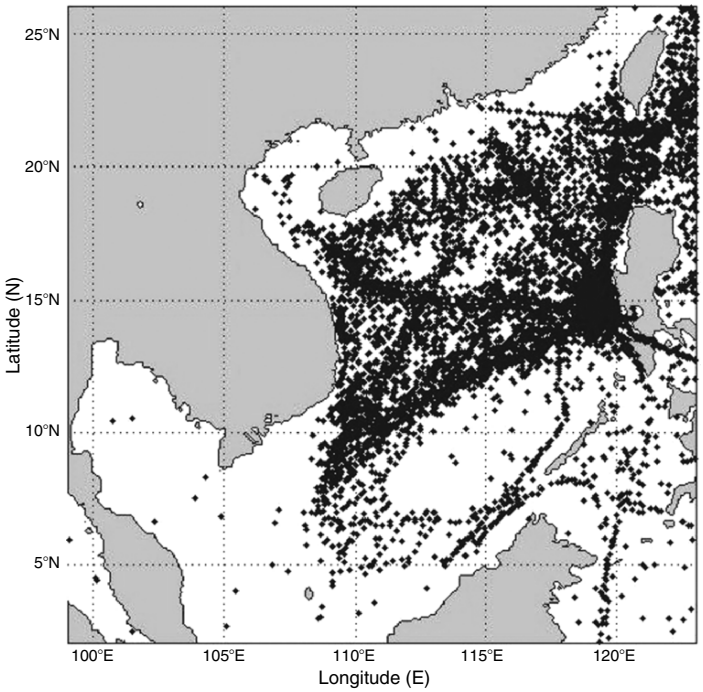


**Fig. 2.29.** Distribution of the MOODS profiles in May 1932–1994 (from Chu et al. 2000a, Journal of Atmospheric and Oceanic Technology)

marked by "*" in Fig. 2.30. Note that the number of "*" in Fig. 2.30 is much less than 40. This is due to several data points sharing the same spots. The 40 MOODS profiles were treated as a test data set. The MOODS data set excluding the test data is the training data set, consisting of 10,113 profiles.

The parametric model (2.34) and the iteration method illustrated in Sect. 2.4.3 are used to obtain a set of thermal parameters $(T_{\mathrm{S}}, T_{\mathrm{tb}}, h_1, h_2, H, G_{\mathrm{th}}, T_{\mathrm{d}})$ for each profile. The thermal parameters are averaged within $1^\circ \times 1^\circ$ grid. The averaged values are taken as the representative values for the grid cell. These values might not be representative in high gradient and coastal regions. Three types of cells were found in the South China Sea, representing co-located MCSST and MOODS data points ("*"), MOODS data points less than ten ("+"), and MOODS data points more than ten ( "o"), as shown in Fig. 2.30.

Usually early May is the time of the summer monsoon onset in the South China Sea (Tao and Chen 1987). The thermal parameters obtained from processing the MOODS data set (May 1932–1994) may represent the thermal response of the South China Sea to the monsoon onset. Figure 2.31 shows the mean thermal parameter fields in May averaged over 1932–1994. Surface warm water (29.5°C) with a maximum temperature 30°C occupies most of

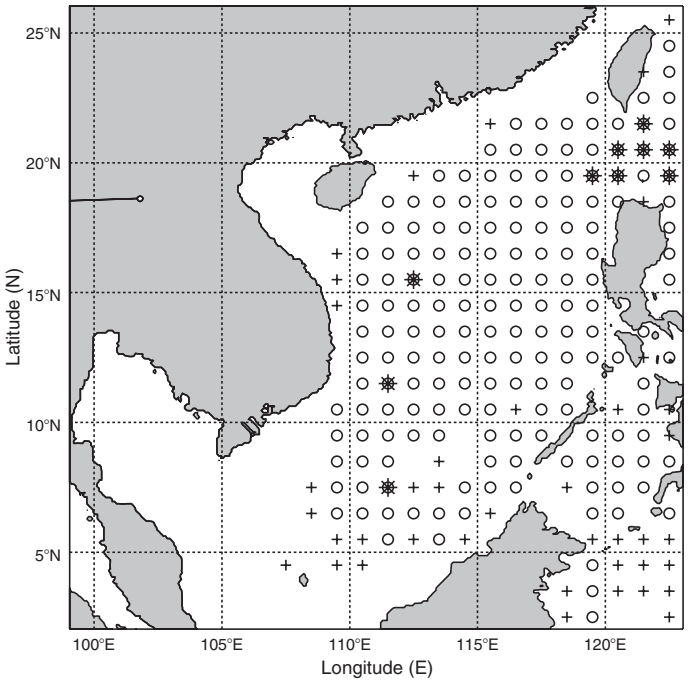


**Fig. 2.30.** Three types of $1^\circ \times 1^\circ$ cells represented by center grid points: co-locating and co-appearing of MCSST and MOODS data points ("*"), MOODS data points less than ten ("+"), and MOODS data points more than ten ("o") (from Chu et al. 2000a, Journal of Atmospheric and Oceanic Technology)

the southern half of the South China Sea (Fig. 2.31a). The 29.5°C isotherm extended from the southeast corner of the Vietnam Coast (near 108°E, 11°N) northeastward to the southwest coast of the Luzon Island (near 120°E, 15°N). $\mathrm{MLD}_T(h_1)$ varied from 10 to 40 m and had a latitudinal variation (Fig. 2.31b).

The southern South China Sea (south of 13°N) was characterized by a deep mixed layer ($h_1 \geq 20\,\mathrm{m}$) region with a maximum value of 40 m near Palawan Island. This suggests strong turbulent mixing in the southern part of the South China Sea immediately after the summer monsoon onset. The northern South China Sea (north of 13°N) has a shallow mixed layer ($h_1 \leq 20\,\mathrm{m}$) with a depth of 10 m. In the continental shelf regions, thermocline bottom depth ($h_2$) was quite shallow ($\leq 100\,\mathrm{m}$) and in the deep South China Sea basin, $h_2$ was deeper ($> 100\,\mathrm{m}$) with a maximum value of 400 m in Luzon Strait (Fig. 2.31c), where however, a weak thermocline ($G_{\mathrm{th}}$) was found with a vertical temperature gradient around $0.04^\circ\mathrm{C\,m^{-1}}$ (Fig. 2.31d). Temperature at $z = -h_2$ ($T_{\mathrm{tb}}$) was coldest (12°C) in Luzon Strait and warmest (22°C) in the southern shelf region near Natuna Island (Fig. 2.31e). The lower layer e-folding thickness ($H$) represents the stratification in the layer below the thermocline. The smaller the value of $H$, the stratification of this layer is

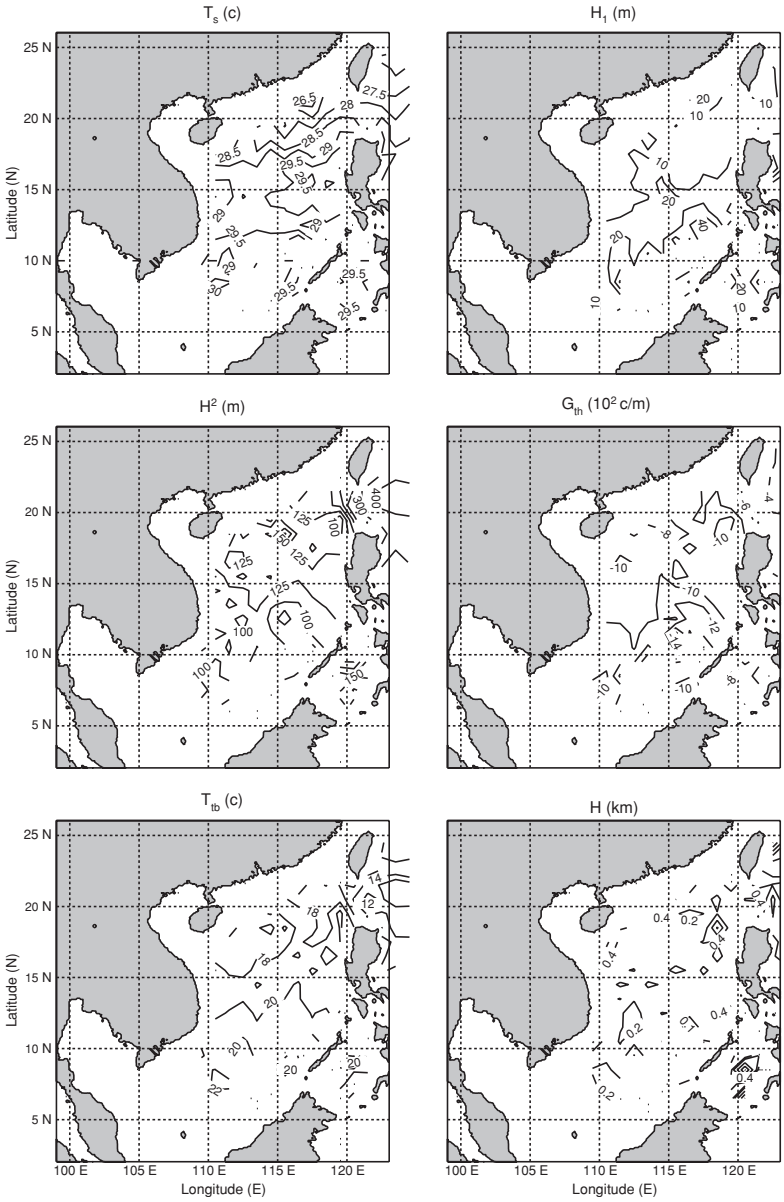


**Fig. 2.31.** Horizontal distributions of mean thermal parameters obtained from the training data set: (**a**) SST, (**b**) $h_1$, (**c**) $h_2$, (**d**) $G_{th}$, (**e**) $T_{tb}$, and (**f**) $H$ (from Chu et al. 2000a, Journal of Atmospheric and Oceanic Technology)

stronger. In the deep basin, $H$ is quite small (100–200 m), indicating weak stratification below the thermocline (Fig. 2.31f). Thus, the South China Sea

thermal response to the monsoon onset can be characterized by a northward advancement of warm surface water, strong turbulent mixing in the southern part with deeper mixed layers, and a relatively uniform deep layer below the thermocline in the deep basin.

### 2.9.3 Regression Method

For each $1^\circ \times 1^\circ$ grid cell, the mean values (for that cell) are subtracted from each of the thermal parameters $(T_\mathrm{S}, T_\mathrm{tb}, h_1, h_2, H, G_\mathrm{th})$ to obtain the thermal parameter anomalies $(T'_\mathrm{S}, T'_\mathrm{tb}, h'_1, h'_2, H', G'_\mathrm{th})$, to compute the correlation coefficients (Table 2.3), and to show the scatter diagrams (Fig. 2.32) between $T'_\mathrm{S}$ and the sub-surface parameter anomalies $(T'_\mathrm{tb}, h'_1, h'_2, H', G'_\mathrm{th})$. Both Table 2.3 and Fig. 2.32 indicate that among the sub-surface parameters, $T'_\mathrm{S}$ has the strongest linear association with $h'_1$. The significance of the correlation can be evaluated by

$$t = \frac{r\sqrt{n-2}}{\sqrt{1-r^2}}, \tag{2.38}$$

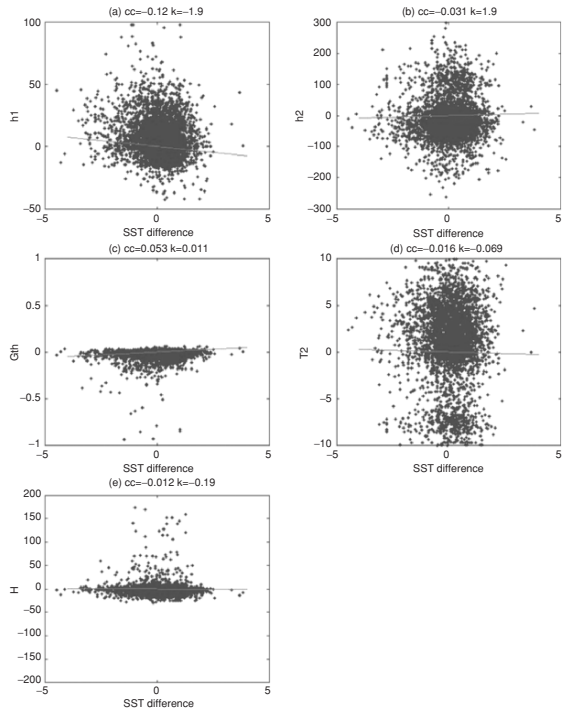


**Fig. 2.32.** Scatter diagrams of SST anomaly with various thermal parameter anomalies: (**a**) $h'_1$, (**b**) $h'_2$, (**c**) $G'_\mathrm{th}$, (**d**) $T'_\mathrm{tb}$, and (**e**) $H'$ (from Chu et al. 2000a, Journal of Atmospheric and Oceanic Technology)

**Table 2.3.** Correlation coefficients with the SST anomaly

| $h_1'$ | $h_2'$ | $G_{\mathrm{th}}'$ | $T_{\mathrm{th}}'$ | $H'$ |
|---|---|---|---|---|
| −0.12 | 0.03 | 0.05 | −0.01 | −0.01 |

**Table 2.4.** The $t$-values of various correlation coefficients

| $h_1'$ | $h_2'$ | $G_{\mathrm{th}}'$ | $T_{\mathrm{th}}'$ | $H'$ |
|---|---|---|---|---|
| −15.77 | 3.98 | 6.64 | −1.33 | −1.33 |

which has a $t$-distribution with $(n-2)$ degrees of freedom. Here, $r$ is the correlation coefficient; $n$ is the number of samples (10,153). We begin with the usual null hypothesis that there is no linear association between $T_{\mathrm{S}}'$ and the sub-surface parameter anomalies $(T_{\mathrm{tb}}', h_1', h_2', H', G_{\mathrm{th}}')$. The critical $t$-value at significance level of 0.005 ($t_{0.005}$) is 2.576. Three absolute values of $t$ computed by (2.38) are larger than the critical value (2.576): −15.77 between $T_{\mathrm{S}}'$ and $h_1'$, 6.64 between $T_{\mathrm{S}}'$ and $G_{\mathrm{th}}'$, and 3.98 between $T_{\mathrm{S}}'$ and $h_2'$ (Table 2.4).

Considering various correlation coefficients (Table 2.3) we may conclude that the correlation between the two short time-scale parameters $T_{\mathrm{S}}'$ and $h_1'$ is stronger than the correlation between $T_{\mathrm{S}}'$ and the long time-scale parameters $(T_{\mathrm{tb}}', h_2', H', G_{\mathrm{th}}')$. This in turn confirms the multi-time-scale hypothesis for the South China Sea thermal parameters.

A negative correlation between $T_{\mathrm{S}}'$ and $h_1'$ might not be true everywhere in the ocean. For example, Tully and Giovando (1963) found it difficult to establish such a relationship at least for a portion of the eastern sub-Arctic Pacific Ocean. However, Chu (1993) pointed out the possibility of such a negative correlation using an analytic ocean mixed layer model for the equatorial Pacific.

For each grid cell, the mean temperature profile, $\bar{T}(z)$, is computed. The temperature anomaly $T'(z)$ is obtained from subtracting the mean profile from each profile in the MOODS training data set. The simplest method of estimating sub-surface $T'(z)$ from $\mathrm{SST}'$ is to regress

$$T'(z) = b(z)\mathrm{SST}', \tag{2.39}$$

where $b(z)$ is the regression coefficient obtained from the training data set.

### 2.9.4 Multi-Time-Scale Method

Having the current SST information in the inversion, we need to use the multi-decorrelation time-scale hypothesis. This hypothesis will reduce the degrees of freedom of the parameter space. The seven parameters vary on different time-scales: $T_{\mathrm{S}}$ and $h_1$ on a short decorrelation time-scale, $T_{\mathrm{tb}}, T_{\mathrm{d}}, h_2, H$, and $G_{\mathrm{th}}$ on a long decorrelation time-scale. The parameters on a long decorrelation time-scale are treated as a background data set which may be pre-determined by historical data. The parameters on the short time-scale are determined by

the inverse method. If the five parameters on the long time-scale are assumed to be pre-determined, the degree of freedom of this model reduces to one. Between the two short time-scale parameters $T_S$ and $h_1$, only one parameter is independent. Usually, we take $T_S$ as the independent parameter. If $T_S$ is given by satellite observation, (2.37) can be used to determine $h_1$, and therefore the vertical profile. This is called the multi-time-scale method. The MOODS data for the South China Sea in May are used to verify this method.

If SST from the MOODS test data (40 data points) (Fig. 2.30) is taken as known values for the short time-scale parameter $T'_S$, we may use (a) the background long time-scale parameters: $T_{tb}, h_2, H, G_{th}$ to determine $h_1$ (Figs. 2.31b,e); or (b) the temperature continuity condition at $z = -h_2$ (2.37) to determine $h_1$; in addition, the May climatological values for $T_d$ (Levitus and Boyer 1994). With all the seven parameters given, vertical profiles $\hat{T}(z)$ can be easily constructed using (2.34). The 40 inverted profiles agree quite well with the observed profiles, however, the 40 regressed profiles have a larger mismatch with the observed profiles (Fig. 2.33).

### 2.9.5 Verification

Any model, including the regression and inverse models presented here, should be verified before claiming any practical usefulness. Usually, the model verification contains two parts: the rms error and the correlation coefficient between modeled and observed profiles.

The May climatological profiles at the MCSST points are used as the "least-effort" profiles. The standard deviation of the climatological profiles represents the first criterion for the model validity. If the model rms error is larger than the climatological standard deviation, the model does not have any practical usefulness. The model becomes valid only if its rms error is smaller than the climatological standard deviation.

Figure 2.34a shows the vertical distribution of the model rms and climatological standard over the whole test data area. The rms errors for both regression and inverse methods increase with depth from the surface to maximum values around 1.8°C near 100 m depth, and then reduce relatively with depth. At all depths except near 100 m depth, the rms errors for the inverse model are smaller than the rms errors for the regression model, which in turn are smaller than the climatological standard deviation. The depth of 100 m is approximately the mean thermocline bottom depth (Fig. 3.31). This implies some difficulty in inverting the temperature at the thermocline bottom depth. Overall, the vertically averaged inverse model ems error (around 0.72°C) is smaller than the regression model rms error (around 1.06°C), which in turn is smaller than the climatological standard deviation (1.51°C).

The correlation coefficients between modeled and observed profiles at all depths represent the second criterion for the model validity. The correlation coefficient for the inverse model varies with depth between 1 and 0.5 and has a vertical mean value of 0.79. Use of (6) leads to $t = 3.559$ for $n = 40$, and

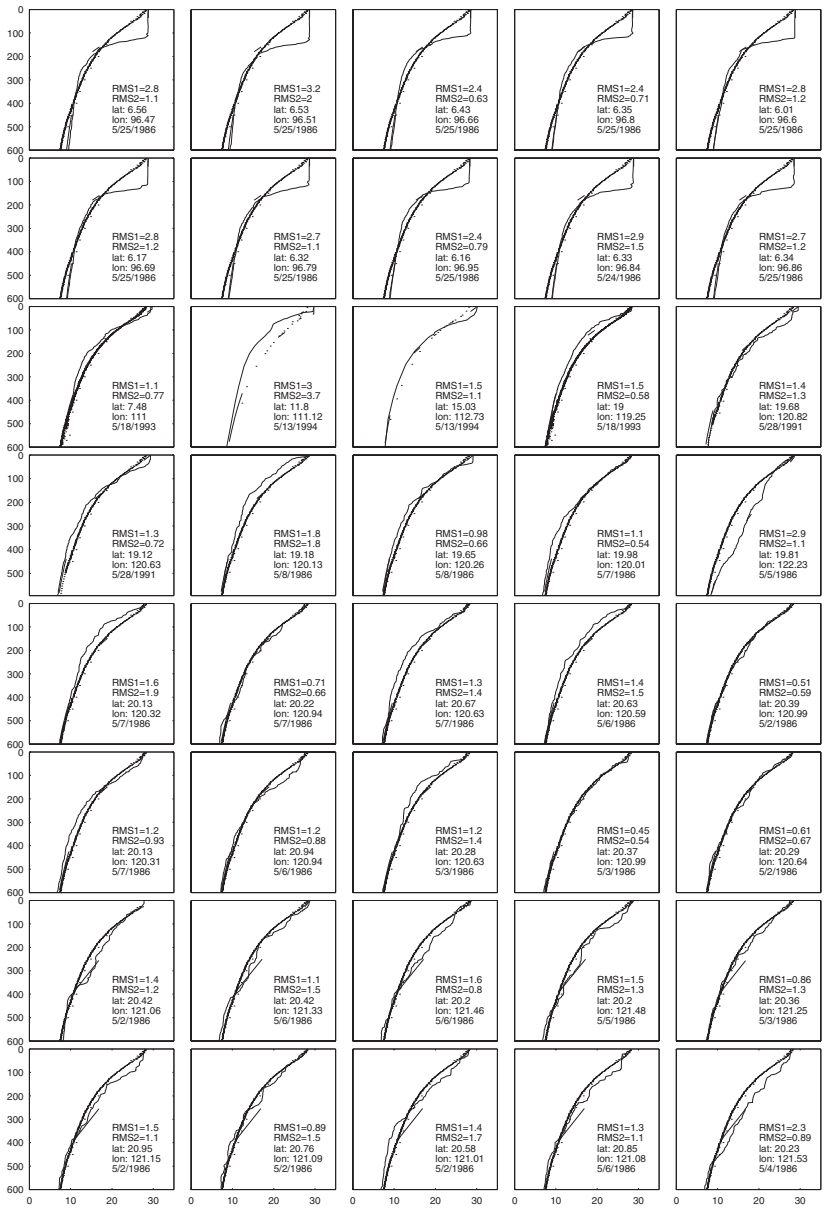


**Fig. 2.33.** Comparison between 40 regressed (*dotted*), inverted (*dash-dotted*), and observed (*solid*) profiles (from Chu et al. 2000a, Journal of Atmospheric and Oceanic Technology)

$r = 0.5$. This value is much larger than the critical $t$-value (2.576), which means significant correlations at confidence level of 0.005 between the in-

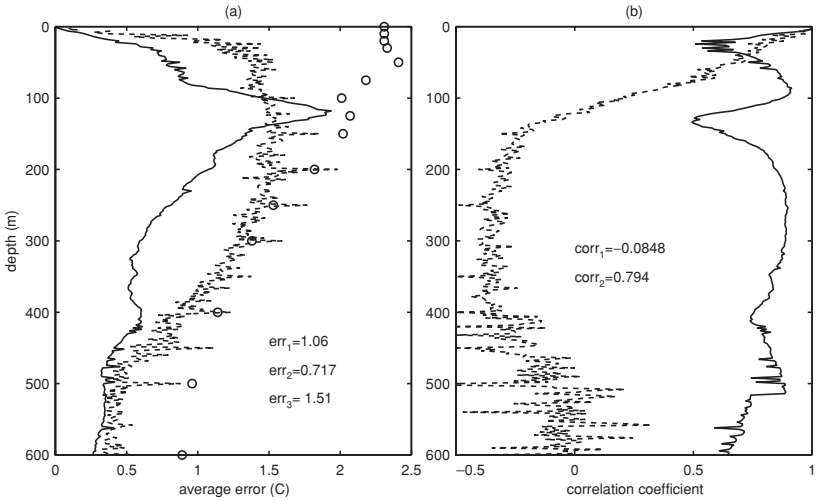


**Fig. 2.34.** Vertical distribution of (**a**) inverse model rms errors (*solid*), regression model rms errors (*dotted*) and climatological standard deviation (*circle*), and (**b**) correlation coefficients between observed and inverted (*solid*), observed and regressed (*dotted*) profiles (from Chu et al. 2000a, Journal of Atmospheric and Oceanic Technology)

verted and the observed profiles for all depths exist. However, the correlation coefficient for the regression model decreases rapidly from one at the surface to zero near 100 m depth, and then becomes negative below that depth (Fig. 2.34b), which indicates no significant positive correlations between the regressed and the observed profiles for the sub-layer depths. The small mean rms error (0.72°C) and high positive correlation coefficient (0.79) make this multi-time-scale inverse method valid for practical use.

### 2.9.6 Limitation of the Multi-Time Scale Hypothesis

The key issue of inverting sub-surface thermal structure from SST is to reduce the degree of freedom of the thermal parameter space by multi-time-scale hypothesis. To apply this method globally, we should first test the validity of this hypothesis. This can be done by the correlation analysis. If correlation between $T'_{\mathrm{S}}$ and $h'_1$ is stronger than the correlation between $T'_{\mathrm{S}}$ and the other parameters $(T'_{\mathrm{tb}}, h'_1, h'_2, H', G'_{\mathrm{th}})$, the multi-time-scale hypothesis is confirmed and the use of this inverse method is feasible. If correlation between $T'_{\mathrm{S}}$ and $h'_1$ is not significant, such as Tully and Giovando (1963) found in one region of the North Pacific, it is very hard to use this method for that region. Furthermore, the rms error and correlation tests should be conducted after the inversion to see the real usefulness.

## 2.10 Autocorrelation Functions

Various ocean systems such as fronts, eddies, and water masses have different temporal and spatial scales. These scales feature a system's life span and spatial extent both horizontally and vertically. For example, White et al. (1982) identified spatial correlation scales in the western Pacific of about 600 km in the tropics (south of 17.5°N) and 300 km in the sub-tropics (north of 17.5°N); Ozsoy et al. (1989) found the spatial scales to be 200–250 km in the Levantine Basin of the Mediterranean Sea; Chu et al. (1997a; 2002b) identified the seasonal variation of the temporal and spatial scales in the Yellow Sea and Sea of Japan (known as the East Sea in Korea) using the autocorrelation function: 90 km from 158 km in winter to 251 km in summer, and the seasonal variation of the surface temporal decorrelation scale is around 2.4 days from 14.7 days in winter to 12.3 days in summer.

The autocorrelation function of $(T, S)$ fields,

$$\eta(l) = \frac{1}{s^2} \int_L \theta'(l_0)\theta'(l_0 + l)\mathrm{d}l_0, \tag{2.40}$$

can be used to represent (temporally and spatially) thermohaline variability. Here, $\theta$ represents temperature or salinity and $\theta'$ is its anomaly; $l_0$ denotes the independent space/time vectors defining the location of points in a sampling space $L$; $l$ is the space/time lag; and $s^2$ is the variance of $\theta$; $\eta$ is computed by paring the anomalies into bins depending upon their separation in space/time, $l$. The values $\eta$ will be obtained from calculating the correlation coefficient for all the anomaly pairs in each bin, which will be constructed for the combination of different lags.

### 2.10.1 Bin Method

For quasi-isolated basin such as the Yellow Sea and the Japan Sea, it is reasonable to assume that the autocorrelation function depends only on the distance between two locations in order to reduce the number of bins. Without this assumption, the number of bins is very large, e.g., 27,000 if each of the temporal and spatial ($x$ and $y$) lags has 30 bins.

Chu et al. (1997a; 2002b) proposed a simple bin method to calculate the autocorrelation function for the East Asian marginal seas such as the Yellow Sea and Sea of Japan. For each observation $\theta_{\mathrm{obs}}$ at depth $z$ (or some equivalent vertical coordinate), the closest grid point climatological value (such as GDEM described in Sect. 3.1.2) $\bar{\theta}_{\mathrm{c}}$ is found and the anomaly,

$$\theta' = \theta_{\mathrm{obs}} - \bar{\theta}_{\mathrm{C}},$$

is computed. Every individual anomaly,$\theta'$, is paired with the other data points, $\hat{\theta}'$, within the temporal domain for analysis (such as same season). The temporal and spatial differences or lags are calculated between the two anomalies.

The anomaly pair $(\theta', \hat{\theta}')$ is then placed in the corresponding temporal lag bin with increment $\Delta t$ (such as one day) and spatial lag bin with increment $\Delta r$ (such as 10 km). If the spatial lag is within $\Delta r_0$ (5 km) and the temporal lag is within $\Delta t_0$ (0.5 day), the corresponding pair is placed into bin (0, 0). If the horizontal lag is between $m\,\Delta r - \Delta r_0$ and $m\,\Delta r + \Delta r_0$, and the temporal lag is between $n\,\Delta t - \Delta t_0$ and $n\,\Delta t + \Delta t_0$, the pair is placed into the bin $(m, n)$ with the pair number $P(m, n)$.

After the anomaly pairs have been spatially and temporally sorted, the autocorrelation function for each bin $(m, n)$ is computed by

$$\eta(m,n) = \frac{\sum_{\text{bin}(m,n)} \theta' \hat{\theta}'}{\sum_{\text{bin}(m,n)} (\theta')^2}, \tag{2.41}$$

which varies with the spatial and temporal lags $(m, n)$. Equation (2.41) indicates that the computed $\eta$ for the bin $(m, n)$ is in fact the estimation of the autocorrelation coefficient of pairs in that bin. A $t$-value for verifying the significance of a sample correlation coefficient is given by (see a statistical text book

$$t = \frac{\eta\sqrt{P-2}}{\sqrt{1-\eta^2}}, \tag{2.42}$$

which is a value of the statistic $T$ having a $t$-distribution with $(P-2)$ degree of freedom. Using $\alpha$ as the level of significance, a criterion $\eta_\alpha$ is obtained

$$\eta_\alpha = \frac{t_\alpha}{\sqrt{P-2+t_\alpha^2}}. \tag{2.43}$$

The estimated autocorrelation function is significant on the level of $\alpha$ if $\eta(m,n) > \eta_\alpha$.

The measured variance $s^2$ is divided into signal $(s_\text{s}^2)$ and noise $(s_\text{n}^2)$ whereby

$$s^2 = s_\text{s}^2 + s_\text{n}^2. \tag{2.44}$$

The noise variance is brought on from two sources, geophysical and instrumentation errors. Here, the geophysical error is unresolved thermal variability with scales smaller than the typical time and space scales between two temperature profiles. In this study the unresolved scales are 0.5 day and 5 km. The autocorrelation function at the first bin (0, 0) does not represent the correlation between profiles paired by themselves, and therefore does not equal one. Following Sprintall and Meyers (1991), the signal-to-noise ratio (SNR) is computed by

$$\lambda = \frac{s_\text{s}}{s_\text{n}} = \sqrt{\frac{\eta(0,0)}{1-\eta(0,0)}}. \tag{2.45}$$

The larger the value of $\lambda$, the less geophysical error exists. If $\eta(0,0) = 1$, there is no noise, $\lambda = \infty$; and if $\eta(0,0) = 0$, there is no signal. If $\lambda > 2$, the ratio of the signal variance,$s_\text{s}^2$, to the noise variance, $s_\text{n}^2$, is greater than four, which is considered quite good conditions by White et al. (1982) and Sprintall and Meyers (1991).

### 2.10.2 Autocorrelation Function in Deep and Shallow Water

Difference is found in calculating the autocorrelation function between deep and shallow (such as continental shelf) water. The deep ocean temperature profiles tend to follow the pattern of mixed layer, a thermocline, and a deeper layer with a slow decrease in temperature with depth. Shallow water does not consistently mimic this pattern. It may range from the classical profile to completely isothermal. The coastal water is largely affected by bathymetry, river run-off, internal waves, and tides. Therefore, the temporal and horizontal scales are also under the strong influence of these forcing factors, and should have different vertical structure from the deep water. For deep waters, the vertical variation of the temporal and horizontal scales are usually obtained from the temperature fields at certain depths (e.g., 100, 200, and 300 m in White et al. 1982) or from SST and the depth of certain temperature (e.g., depth of 20°C in Sprintall and Meyers (1991). For deep water, these depths are easily determined (Fig. 2.35a).

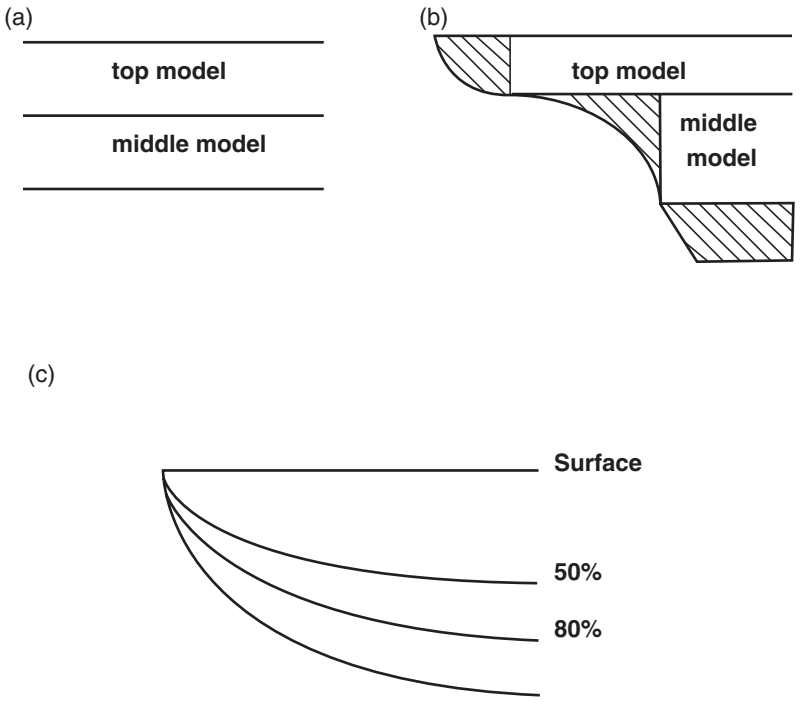


**Fig. 2.35.** Depths for computing autocorrelation function for the Yellow Sea: (**a**) horizontal levels for deep water, (**b**) horizontal levels for continental shelf, and (**c**) bottom following levels (from Chu et al. 1997a, Journal of Geophysical Research)

### 2.10.3 Shallow Water – Yellow Sea Temperature Field

(a) Topographic – following level. For shallow water (such as the Yellow Sea, see Fig. 2.6), horizontal and temporal scales should not be identified at given depths. This is because a single layer structure in the Yellow Sea appearing in winter, which makes the depth of certain isotherm non-representative for the sub-surface thermal fields; and because of a strong influence of horizontally varying bathymetry on the shallow water, which causes the temperature fields at different depths to be non-representative of sub-surface fields. A sloping bottom for shallow water, any chosen depths will lead to some areas (hashed area in Fig. 2.35b) not covered by any sub-models. Therefore, it is more reasonable to calculate the autocorrelation function at terrain-following coordinate,

$$\sigma_{\text{topo}} = -\frac{z}{H}. \tag{2.46}$$

Here $H$ is the water depth, and $z$ is the vertical coordinate. Mid-water properties are represented by $\sigma_{\text{topo}} = 5$, and the near-bottom water features are portrayed by $\sigma_{\text{topo}} = 8$ (Fig. 2.35c). The analysis on the $\sigma_{\text{topo}}$-coordinate system benefits initializing popular $\sigma_{\text{topo}}$-coordinate coastal models, such as the Princeton Ocean Model (Blumberg and Mellor 1987), but has disadvantage during weakly forced and stratified periods. The deeper $\sigma_{\text{topo}}$-levels will be within the mixed layer environment in shoal areas and below the mixed layer in the deeper portions of the basin.

(b) Pair-number. The MOODS data have approximately 35,658 profiles (during 1929–1991) for the Yellow Sea shelf. The pair-number distributions, $P(m, n)$, for the four seasons are depicted in Fig. 2.36. Uneven distribution is seen in the temporal and spatial bins. Almost everywhere $P(m, n)$ is equal or more than 500. The maximum $P(m, n)$ is located in bins with near 1–2 day temporal lags and 80–120 km spatial lags.

Since the pair-number for each bin, $P(m, n)$, is given, the criterion for the autocorrelation function $(\eta_\alpha)$ for a particular level of significance $(\alpha)$ can be calculated using (2.43). The criterion $\eta_\alpha$ has a strong seasonal variation (Fig. 2.37) due to the change of pair numbers $P(m, n)$. It is smaller for most bins in summer than in winter. Figure 2.38 shows the dependence of $\eta(m, n)$ on the temporal and spatial lags in winter and summer. The autocorrelation function decreases with temporal and spatial lags faster in winter than in summer.

When

$$\eta^{(\sigma)}(m, n) > \eta_\alpha, \tag{2.47}$$

the estimated autocorrelation function is significant on the level of $\alpha$. Since both $\eta^{(\sigma)}(m, n)$ and $\eta_\alpha$ have seasonal variations, the significance level should also be changed with seasons. The significant surface autocorrelation function estimation ($\alpha = 0.10$) is limited to the left lower corner of the $(\tau, r)$ plane with $\tau < 15$ day and $r < 200$ km in winter (Fig. 2.37a) and occupies nearly the whole left part of the $(\tau, r)$ plane with $\tau < 20$ day in summer (Fig. 2.37b).

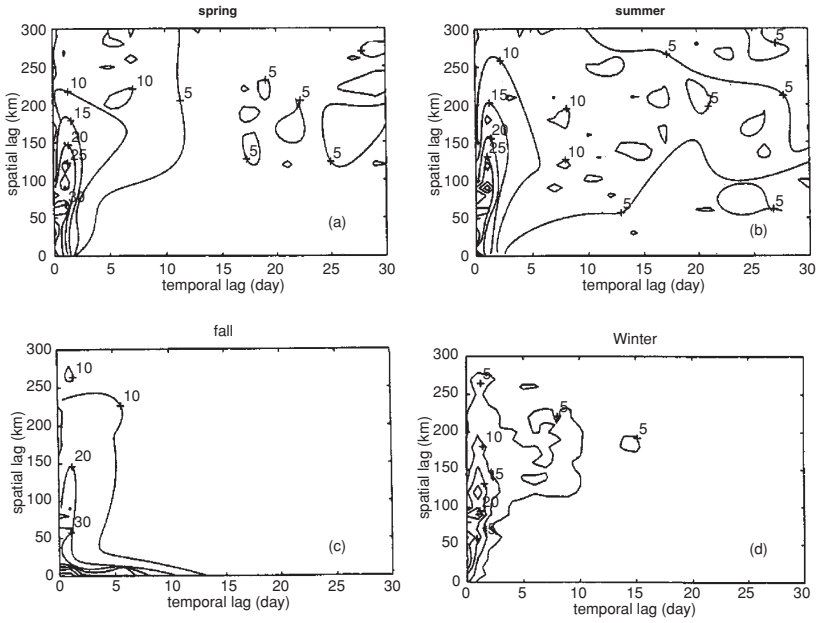


**Fig. 2.36.** The pair-number (in 100) distribution in the $(m, n)$ space of the Yellow Sea for (**a**) spring, (**b**) summer, (**c**) fall, and (**d**) winter (from Chu et al. 1997a, Journal of Geophysical Research)

Such a seasonal variability in significant autocorrelation function estimations leads to a significant difference in statistical parameters such as decorrelation scales.

(c) Temporal lag. After the anomaly pairs have been spatially and temporally sorted, the autocorrelation function of temperature is computed using (2.41). Temporal dependence of the autocorrelation $\eta^{(\sigma)}(m, n)$ can be easily discussed by $\eta - n$ curves at several different spatial lags, e.g., $m = 0$ ("no lag"), $m = 1$ (10 km lag), and $m = 15$ (150 km lag). These curves are plotted for different seasons and three $\sigma_{\text{topo}}$ levels (0, 0.5, and 0.8) in order to see the seasonal and vertical variations. The three winter curves, $\eta^{(\sigma)}(0, n)$, $\eta^{(\sigma)}(1, n)$, and $\eta^{(\sigma)}(15, n)$, are plotted for the surface, $\sigma_{\text{topo}} = 0$ (Fig. 2.39a), the mid-level, $\sigma_{\text{topo}} = 0.5$ (Fig. 2.39b), and the near-bottom, $\sigma_{\text{topo}} = 0.8$ (Fig. 2.39c).

The three summer curves, $\eta^{(\sigma)}(0, n), \eta^{(\sigma)}(1, n)$, and $\eta^{(\sigma)}(15, n)$ are plotted for the surface, $\sigma_{\text{topo}} = 0$ (Fig. 2.40a), the mid-level, $\sigma_{\text{topo}} = 0.5$ (Fig. 2.40b), and the near-bottom, $\sigma_{\text{topo}} = 0.8$ (Fig. 2.40c). The autocorrelation function has the following features: (1) Its temporal variability weakens as the spatial lag increases, and becomes extremely small (near constantly low values) at the spatial lag $m = 15$ (150 km) except for the summer surface field (Fig. 2.40a), where it decreases quasi-linearly with the time lag (dotted curve line in Fig. 2.40a). (2) Its vertical variability is quite small during

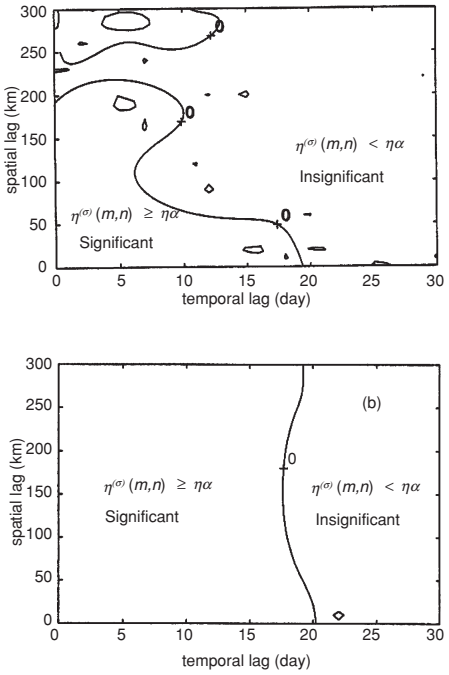


**Fig. 2.37.** Criterion ($\alpha = 0.10$) for the surface autocorrelation function estimation in the Yellow Sea: (**a**) winter, and (**b**) summer (from Chu et al. 1997a, Journal of Geophysical Research)

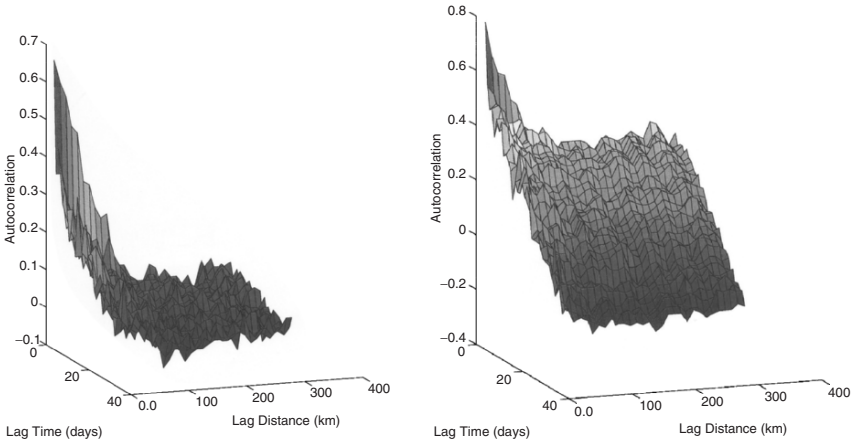


**Fig. 2.38.** Dependence of autocorrelation function $\eta$ for the Yellow Sea temperature field on the temporal and spatial lags: (**a**) winter, and (**b**) summer. Note that the decrease of $\eta$ with lag is faster in winter than in summer

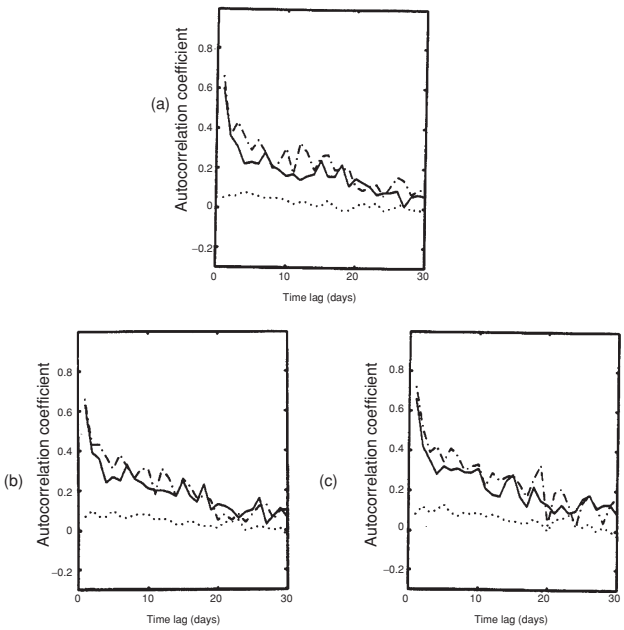


**Fig. 2.39.** Winter temporal variation of autocorrelation function at different spatial lags: $m = 0$ (no lag, *dash-dot curve*), $m = 1$ (10 km lag, *solid curve*), and $m = 15$ (150 km lag, *dotted curve*) for three levels: (**a**) surface ($\sigma_{\text{topo}} = 0$)), (**b**) mid-level ($\sigma_{\text{topo}} = 0.5$), and (**c**) near bottom ($\sigma_{\text{topo}} = 0.8$) (from Chu et al. 1997a, Journal of Geophysical Research)

winter (Fig. 2.39) and not so small during summer (Fig. 2.40). This coincides with the single-layer structure in winter and the multi-layer structure in summer (see Sect. 2.4). (3) During summer its temporal variability weakens with depth. The surface autocorrelation function shows a fast reduction with time lag $n$ (Fig. 2.40a). At mid-level ($\sigma_{\text{topo}} = 0.5$), it has slower reduction than the surface as $n$ increases (Fig. 2.40b). At near-bottom ($\sigma_{\text{topo}} = 0.8$), it fluctuates around certain values (0.5 for no-spatial lag, 0.28 for 10 km lag, and almost 0 for 150 km) as $n$ increases (Fig. 2.40c).

(d) Spatial lag. The spatial dependence of autocorrelation function,$\eta^{(\sigma)}(m, n)$, can be easily discussed by $\eta - m$ curves at several different temporal lags, e.g., $n = 0$ (no lag), $n = 1$ (one day lag), and $n = 15$ (15 day lag). These curves are plotted for different seasons and three $\sigma_{\text{topo}}$ levels (0, 0.5, and 0.8) in order to see the seasonal and vertical variations. The three winter curves,$\eta^{(\sigma)}(m, 0), \eta^{(\sigma)}(m, 1)$, and $\eta^{(\sigma)}(m, 15)$, are plotted for the surface, the surface, $\sigma_{\text{topo}} = 0$ (Fig. 2.41a), the mid-level, $\sigma_{\text{topo}} = 0.5$ (Fig. 2.41b), and the near-bottom, $\sigma_{\text{topo}} = 0.8$ (Fig. 2.41c).

The three summer curves, $\eta^{(\sigma)}(m, 0), \eta^{(\sigma)}(m, 1)$, and $\eta^{(\sigma)}(m, 15)$, are plotted for the surface, $\sigma_{\text{topo}} = 0$ (Fig. 2.42a), the mid-level, $\sigma_{\text{topo}} = 0.5$

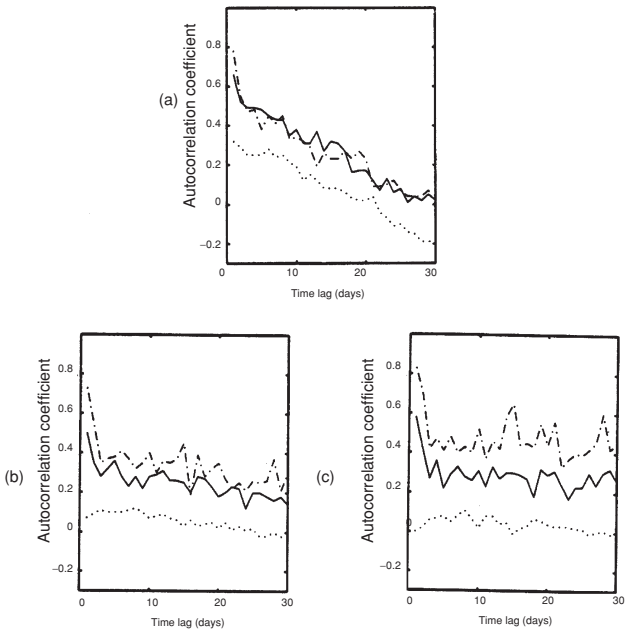


**Fig. 2.40.** Summer temporal variation of autocorrelation function at different spatial lags: $m = 0$ (no lag, *dash-dot curve*), $m = 1$ (10 km lag, *solid curve*), and $m = 15$ (150 km lag, *dotted curve*) for three levels: (**a**) surface ($\sigma_{\text{topo}} = 0$), (**b**) mid-level ($\sigma_{\text{topo}} = 0.5$), and (**c**) near bottom ($\sigma_{\text{topo}} = 0.8$) (from Chu et al. 1997a, Journal of Geophysical Research)

(Fig. 2.42b), and the near-bottom, $\sigma_{\text{topo}} = 0.8$ (Fig. 2.42c). The autocorrelation function has the following features: (1) Its spatial variability weakens as the temporal lag increases, and becomes very small (smaller than 0.2) at the time lag $n = 15$ day except for the summer near-bottom field (Fig. 2.42c), where the horizontal variability of the autocorrelation function at $n = 15$ day is quite close to that at $n = 0$ (no time lag) and $n = 1$ day lag, as shown in Fig. 2.42c. This indicates that during summer the tidal effect (on the time-scale is less or equal than one day) is important for the Yellow Sea bottom thermal field. (2) Its vertical variability is quite small during the winter (Fig. 2.41) and not so small during the summer (Fig. 2.42). This coincides with the single-layer structure in the winter and the multi-layer structure in the summer months (see Sect. 2.4.2). (3) During summer, the spatial variability of the autocorrelation function strengthens with depth. The surface autocorrelation function shows a relatively weak reduction versus spatial lag (Fig. 2.42a). The mid-level ($\sigma_{\text{topo}} = 0.5$) autocorrelation function has a stronger reduction than the surface as the spatial lag increases (Fig. 2.42b). The near-bottom ($\sigma_{\text{topo}} = 0.8$) autocorrelation function has the strongest reduction versus spatial lag (Fig. 2.42c).

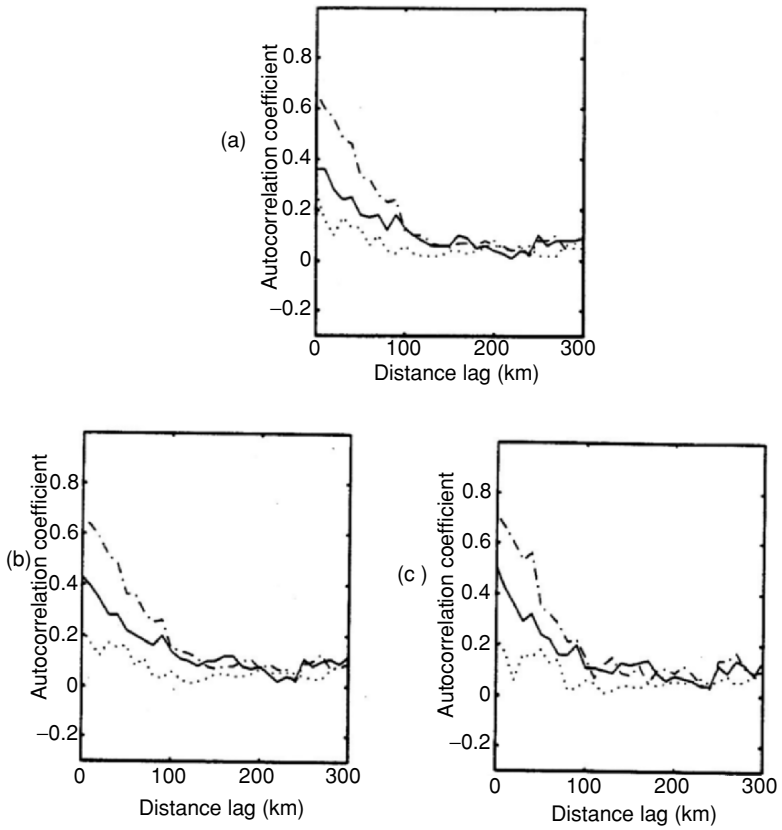


**Fig. 2.41.** Winter spatial variation of autocorrelation function at different temporal lags: $n = 0$ (no lag, *dash-dot curve*), $n = 1$ (one day lag, *solid curve*), and $n = 15$ (15 day lag, *dotted curve*) for three levels: (**a**) surface ($\sigma_{\text{topo}} = 0$), (**b**) mid-level ($\sigma_{\text{topo}} = 0.5$), and (**c**) near bottom ($\sigma_{\text{topo}} = 0.8$) (from Chu et al. 1997a, Journal of Geophysical Research)

## 2.11 Temporal and Spatial Decorrelation Scales

Various ocean systems such as fronts, eddies, and water masses have different temporal and spatial scales. These scales feature a system's life span and spatial extent both horizontally and vertically. For example, White et al. (1982) identified spatial decorrelation scales in the western Pacific of about 600 km in the tropics (south of 17.5°N) and 300 km in the sub-tropics (north of 17.5°N) while Ozsoy et al. (1989) found the spatial scales to be 200–250 km in the Levantine Basin of the Mediterranean Sea. Chu et al. (1997a; 2002b) use the Gaussian model to fit the autocorrelation function and then to identify the decorrelation scale as the scale for the spatial or temporal variability.

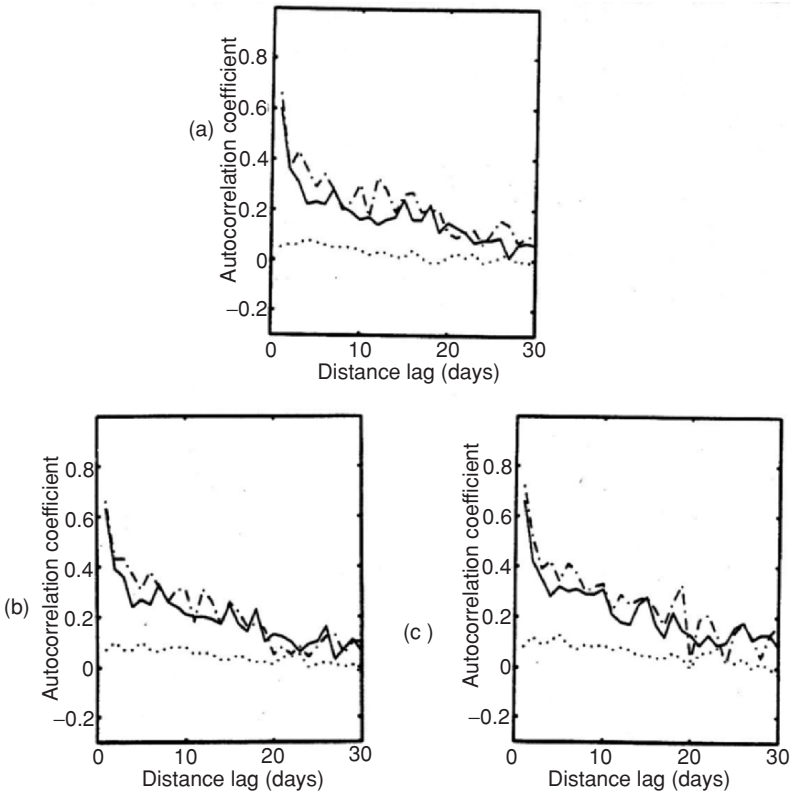


**Fig. 2.42.** Summer spatial variation of autocorrelation function at different temporal lags: $n = 0$ (no lag, *dash-dot curve*), $n = 1$ (one day lag, *solid curve*), and $n = 15$ (15 day lag, *dotted curve*) for three levels: (**a**) surface ($\sigma_{\text{topo}} = 0$), (**b**) mid-level ($\sigma_{\text{topo}} = 0.5$), and (**c**) near bottom ($\sigma_{\text{topo}} = 0.8$) (from Chu et al. 1997a, Journal of Geophysical Research)

### 2.11.1 Gaussian Model

The Gaussian model

$$\hat{\eta}^{(\sigma)}(m,n) = \hat{\eta}^{(\sigma)}(0,0) \exp\left[-A_\sigma^2 (m\,\Delta r)^2 - C_\sigma^2 (n\,\Delta\tau)^2\right], \tag{2.48}$$

is often used to fit the autocorrelation function (Clancy and Pollak 1983; Phoebus 1988; Chu et al. 1997a; 2002b). Here, $\hat{\eta}^{(\sigma)}(m,n)$ denotes the Gaussian fit of the autocorrelation function at the level $\sigma_{\text{topo}}$ in the bin with the spatial separation $m\,\Delta r$, and the temporal separation $n\,\Delta\tau$ with $(\Delta r, \Delta\tau)$ the increments for the space/time separation. $A_\sigma^{-1}$ and $C_\sigma^{-1}$ are horizontal and temporal decorrelation scales at the level $\sigma_{\text{topo}}$. The dominant space/time scales obtained from the autocorrelation function are important not only in determining sampling density but also for the optimum interpolation of the

observed data. For example, the US Navy's Optimal Thermal Interpolation System runs everyday, combines real-time data, climatology, and predictions from ocean mixed layer models to represent an accurate picture of the ocean thermal structure on global and regional scales (Phoebus 1988; Clancy and Pollak 1983). Before running this system, the temporal and spatial scales, $A_\sigma^{-1}$ and $C_\sigma^{-1}$, should specify.

### 2.11.2 *F*-Test for the Gaussian Model

One can test the null hypothesis $H_0$ to indicate that the Gaussian model (2.48) is not significant by merely forming the ratio (see any statistics book)

$$F = \frac{\text{SSR}/k}{\text{SSE}/(l-k-1)}, \tag{2.49}$$

where $k = 2$, $l$ is the total number of bins in either spatial or temporal lags, and

$$\text{SSR} = \sum_m \sum_n \left[\ln \hat{\eta}^{(\sigma)}(m,n) - \text{mean}(\ln \hat{\eta}^{(\sigma)}(m,n))\right]^2, \tag{2.50}$$

$$\text{SSE} = \sum_m \sum_n \left[\ln \hat{\eta}^{(\sigma)}(m,n) - \ln \eta^{(\sigma)}(m,n)\right]^2, \tag{2.51}$$

denote a regression sum of squares and a residual mean square, respectively. When

$$F > F_\alpha(k, l-k-1), \tag{2.52}$$

the null hypothesis $H_0$ is rejected. The Gaussian model is significant. Here $F_\alpha(k, l-k-1)$ satisfies the $F$-distribution with $\nu_1 = k$, $\nu_2 = l-k-1$, and a confidence level of $\alpha$. The $F$-values for different levels and seasons are listed in Table 2.5. All the $F$-values exceed the critical value (5.45) of the $F$-distribution for 2 and 28 degrees of freedom at $\alpha = 0.01$. Therefore, the Gaussian model is reasonable for the Yellow Sea thermal autocorrelation function.

### 2.11.3 Seasonal Variability of the Decorrelation Scales

The computed autocorrelation function for different seasons and levels ($\sigma_{\text{topo}} =$ 0, 0.5, 0.8) are then fitted to a Gaussian function of the form of (2.48) by the regression method, which lead to the spatial and temporal decorrelation scales,

**Table 2.5.** $F$-values for estimating the Yellow Sea autocorrelation function

| $\sigma_{\text{topo}}$−level | winter | summer |
|---|---|---|
| surface | 28.64 | 12.26 |
| 0.5 | 26.43 | 11.71 |
| 0.8 | 25.01 | 11.34 |

**Table 2.6.** Seasonal and vertical variations of decorrelation scales of the Yellow Sea

| Season | Level | temporal scale (day) | spatial scale (km) | SNR ($\lambda$) |
|---|---|---|---|---|
| Winter | 0 | 14.7 | 158 | 2.06 |
| | 0.5 | 14.7 | 167 | 1.88 |
| | 0.8 | 15.2 | 172 | 2.21 |
| Summer | 0 | 12.3 | 251 | 3.00 |
| | 0.5 | 15.8 | 169 | 2.21 |
| | 0.8 | 17.2 | 157 | 3.00 |

$A_\sigma^{-1}$ and $C_\sigma^{-1}$, respectively. Table 2.6 presents these decorrelation scales and SNRs for winter and summer.

The SNR for both winter and summer are higher than that for the deep waters of the Eastern Equatorial Pacific, which is around 1.0 as reported by Sprintall and Meyers (1991). This infers that the temperature signal in the Yellow Sea shelf is stronger than in the open waters. In both winter and summer seasons, the largest noise occurs at the mid-level ($\sigma_{\text{topo}} = 0.5$). This is expected since this is the transition layer where both the meteorological and topographic effects occur. The SNR is greater in summer than in winter.

The vertical variation in temporal and spatial decorrelation scales is smaller in winter than in summer. In winter, the temporal scale varies only a half-a-day and the horizontal scale changes only 14 km among three different levels ($\sigma_{\text{topo}} = 0, 0.5, 0.8$). This vertically quasi-uniformity in decorrelation scales also represents the winter single-layer structure caused by the strong surface forcing. In the winter season, the Yellow Sea shelf has strong mixing due to both strong winds and the upward buoyancy flux. With a large part of the Yellow Sea having depths less than 50 m, vertical mixing reaches the bottom and creates isothermal profiles. Thus, decorrelation scales will be similar from the surface to the near-bottom ($\sigma_{\text{topo}} = 0.8$) water column. In summer, the temporal scale increases five days and the horizontal scale decreases 94 km from the surface ($\sigma_{\text{topo}} = 0$) to the near-bottom ($\sigma_{\text{topo}} = 0.8$) waters. This vertically varying decorrelation scales also implies the summer multi-layer structure.

Surface horizontal decorrelation scales are almost 100 km longer in summer than in winter. This is due to the strong solar heating in summer, causing a relatively uniform SST field. Surface temporal decorrelation scales are 2.4 days shorter in summer than in winter. This might be caused by the shallower surface mixed layer in summer (less thermal inertia). Only the upper layer water is affected in summer by the atmospheric forcing rather than the entire water column as in winter. The surface temporal decorrelation scale should be shorter in summer than in winter.

An interesting feature shown in Table 2.6 is the increase of temporal decorrelation scale with depth in both summer (evident) and winter (slight). The near-bottom water ($\sigma_{\text{topo}} = 0.8$) has the longest temporal scale in summer,

which could be directly related to the existence of the Yellow Sea Cold Water throughout the summer in the middle of the Yellow Sea.

### 2.11.4 Usefulness of the Decorrelation Scales

The decorrelation scales are widely used in the OI system to map irregular data into regular grid points and in the observational system design to determine the horizontal and temporal resolution of the observational network. Since interpolating irregular data into regular grid points will be discussed in the next chapter, we only discuss the application to the observational network design.

As mentioned in Sect. 2.10.1, the noise comes from instrumental and geophysical errors. Since the instrumental error in XBT measurements is usually about 0.1°C (Barnett and Bernstein 1980), and even smaller in CTD measurements, the instrumental error is generally neglected against the geophysical error. This implies that the curtailment of noise must be accomplished by the reduction of geophysical error. This is usually done by increasing the sample density. Having determined the statistical structure of thermal variability in the Yellow Sea shelf, the minimum sampling density required to detect thermal variability can now be arbitrated as two or three samples per decorrelation scale (Sprintall and Meyers 1991). This would mean that spatially, any temperature measurement in both summer and winter may be conducted at 50–80 km and 4–6 day intervals with the knowledge that the sub-surface features will also be adequately sampled.

### Questions and Exercises

(1) What are the major features of the ocean observational data such as CTD, XBT, or AXBT measurements?
(2) What are the two kinds of representation of a temperature (or salinity) profile? What are the advantages and disadvantages of using each representation?
(3) When are the major characteristics of the thermal parametric model for the non-polar regions depicted in Fig. 2.8? How many independent parameters are there in this thermal parametric model?
(4) When are the major characteristics of the thermal and haline parametric models for the polar region depicted in Figs. 2.13 and 2.14? How many independent parameters are there in this thermal parametric model?
(5) For the polar region, what are the major differences of the ($T$, $S$) profiles among the shallow-mixing, deep-mixing, and advection-types?
(6) What are the major differences between parametric and curve-fitting models? Please discuss the advantages and disadvantages of each model.
(7) What are the objective and subjective determination of ocean mixed layer depth? What is the major difficulty in objective determination of the mixed layer depth from the profile data?

(8) There are two types of criteria (difference and gradient) in subjective determination of the mixed layer depth. Please discuss the difference between the two.
(9) Work with your ($T$, $S$) profiles such as XBT measurements. Please (a) compute the second derivatives $\partial^2 F(z_j)/\partial z^2$ ($F$ is $T$ or $S$) using (2.6) and determine the mixed layer depth objectively; (b) determine the mixed layer depth subjectively using the difference criterion (2.26a) or (2.26b); (c) determine the mixed layer depth subjectively using the gradient criterion (2.26c). Compare the three sets of the mixed layer depth data and discuss the difference among them.
(10) Under what conditions, the subjective (difference and gradient) and objective methods will cause large errors?
(11) Two approaches exist to establish climatological mean mixed layer depth field: (a) determine the mean mixed layer depth from the climatological mean ($T$, $S$) profiles, (b) the synoptic mixed layer depth from observational ($T$, $S$) profiles and then average the synoptic mixed layer depth to get the climatological mean mixed layer depth (described in Sect. 2.7.2). Why is the mixed layer determined from the first approach always larger than that from the second approach? If you want to build up climatological mean mixed layer depth (or thermocline/halocline depth), which approach will you take? Why?
(12) From the time-longitude plot of monthly mean mixed layer depth in the equatorial Pacific (Fig. 2.18), what kinds of wave motion can be identified?
(13) What is the barrier layer? What are the major mechanisms causing the barrier layer? Why?
(14) Can barrier layer occur in high latitude oceans? Why?
(15) What are the major difficulties to determine temperature profile from SST? What is the advantage to use the multiple time-scale method?
(16) What errors do you make when you use the bin method (2.41) to calculate the autocorrelation function $\eta$ defined by (2.40)? Why?
(17) What is the difference between deep and shallow water in computing the autocorrelation function from observational ($T$, $S$) profiles? Why?
(18) What is the limitation of using the Gaussian model to fit the autocorrelation function computed from the observed ($T$, $S$) profiles?

$$\hat{\eta}^{(\sigma)}(m,n) = \hat{\eta}^{(\sigma)}(0,0)\exp\left[-A_\sigma^2(m\,\Delta r)^2 - C_\sigma^2(n\,\Delta\tau)^2\right]$$

(19) Discuss the usefulness and application of the autocorrelation function and associated decorrelation scales.